Geophysical Journal International

Geophys. J. Int. (2018) **215,** 133–154
Advance Access publication 2018 July 07
GJI Seismology

doi: 10.1093/gji/ggy273

An SEM-DSM three-dimensional hybrid method for modelling teleseismic waves with complicated source-side structures

Wenbo Wu,[1,2] Sidao Ni,[1] Zhongwen Zhan[3] and Shengji Wei[4,5]

[1] *State Key Laboratory of Geodesy and Earth's Dynamics, Institute of Geodesy and Geophysics, Chinese Academy of Sciences, Wuhan* 430077, *China*
[2] *Department of Geosciences, Princeton University, Princeton, NJ* 08541, *USA. E-mail: sdni@whigg.ac.cn*
[3] *Seismological Laboratory, California Institute of Technology, Pasadena, CA* 91125, *USA*
[4] *Earth Observatory of Singapore, Nanyang Technological University, Singapore* 639798, *Singapore*
[5] *Asian School of Environment, Nanyang Technological University, Singapore* 639798, *Singapore*

Accepted 2018 July 5. Received 2018 January 7; in original form 2018 June 30

SUMMARY

Despite recent advances in High Performance Computing (HPC), numerical simulation of high frequency (e.g. 1 Hz or higher) seismic wave propagation at the global scale is still prohibitive. To overcome this difficulty, we propose a hybrid method to efficiently compute teleseismic waveforms with 3-D source-side structures. By coupling the Spectral Element Method (SEM) with the Direct Solution Method (DSM) based on the representation theorem, we are able to limit the costly SEM simulation to a small source-side region and avoid computation over the entire space of the Earth. Our hybrid method is benchmarked against 1-D DSM synthetics and 3-D SEM synthetics. We also discuss numerical difficulties in the implementation, including slow DSM convergence near source depth, discretization error, Green's function interpolation and local 3-D wavefield approximations. As a case study, we apply our hybrid method to two subduction earthquakes and show its advantage in understanding 3-D source-side effects on teleseismic *P*-waves. Our hybrid method reduces computational cost by more than two orders of magnitude when only source-side 3-D complexities are of concern. Thus our hybrid method is useful for a series of problems in seismology, such as imaging 3-D structures of a subducting slab or a mid-ocean ridge and studying source parameters with 3-D source-side complexities using teleseismic waveforms.

Key words: wave propagation; body waves; computational seismology; earthquake dynamics; seismicity and tectonics.

1 INTRODUCTION

Seismic structures of mid-ocean ridges and subduction zones are very complicated due to interaction of various active processes. For example, mid-ocean ridges usually feature complicated seafloor relief beneath a few kilometres of water. Structures of subduction zones are even more complex. The complexities include a water layer of rapidly varying depth, the juxtaposition of continental and oceanic crust, and thick sediments (Fig. 1). Even subducted slab itself is seismically heterogeneous deep into the Earth. Lateral variations of velocity structures, topography, and bathymetry present in subduction zones are among the strongest on the planet and may produce substantial waveform complexities at global (Okamoto 1993, 1994; Okamoto & Takenaka 2009) and regional scales. These waveform complexities lead to difficulty in modelling teleseismic waves, both for studies of earthquake source parameters and velocity structures.

Moreover, the majority of the large earthquakes occur in subduction zones, yet the constraints on source parameters of offshore events usually suffer larger uncertainties than inland events due to more complex structures and one-sided regional station distribution. Traditionally, teleseismic body-wave records have been broadly used in constraining source locations, focal mechanism or finite fault ruptures, because a large distance range spanned by teleseismograms includes many stations with favourable azimuthal distribution. However, near-source 3-D effects may strongly influence teleseismic records, especially for earthquakes close to trenches. These strong 3-D effects could bias the source parameter estimations, which are mostly derived by fitting data with 1-D synthetics. For example, Lee *et al.* (2016) reported obvious late signals in teleseismic *P*-waves of the 2015 M_w8.4 Illapel earthquake and attributed them to a second stage of rupture process. However, it has been proposed that a substantial portion of slip may occur near the trench (Melgar *et al.* 2016), and an alternative interpretation for the late signals is strong codas of *P*-waves due to 3-D effects. Indeed, delayed ruptures or early large aftershocks of great earthquakes have attracted attention from many researchers (Fan & Shearer 2016; Lay *et al.* 2016; Lee *et al.* 2016). To resolve these issues, 3-D effects near the

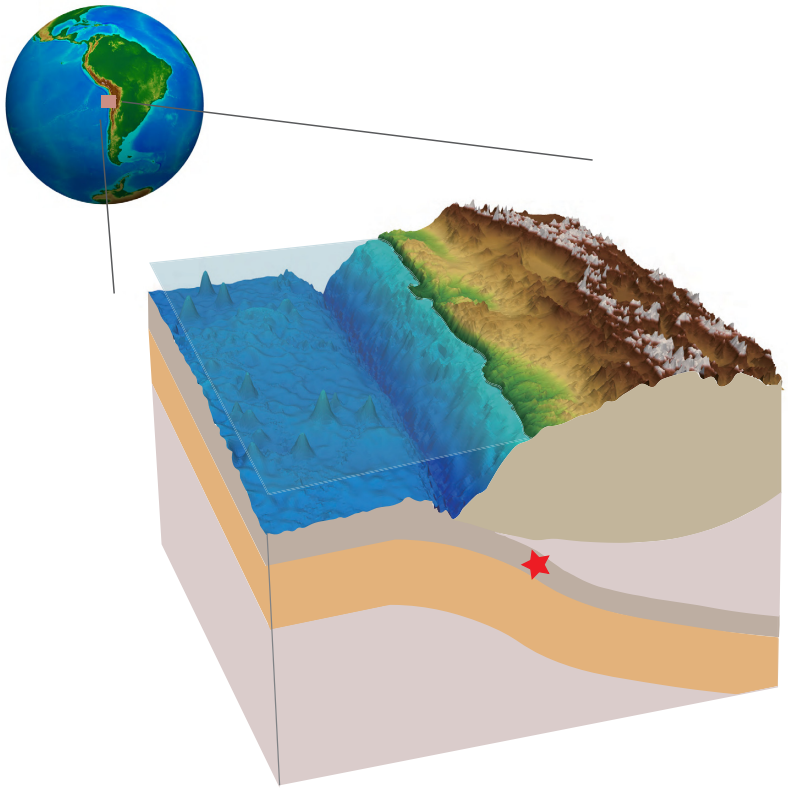

Figure 1. Schematic cartoon to illustrate the complex 3-D structures near the Peru–Chile trench. The topography/bathymetry features are real, but exaggerated for visualization. The red star represents an earthquake close to the trench.

source-side should be quantified, given that the actual topography/bathymetry are accurately known and marine sediments for some particular regions are also known well from active-source reflection/refraction profiles.

Apart from earthquake source inversions, teleseismic body waves can also be used to investigate source-side structures near subduction zones and mid-ocean ridges. Of course, with a dense ocean bottom seismic array or an active-source seismic survey, imaging of high-resolution 3-D structures is possible. Unfortunately, vast ocean regions are not well instrumented. However, teleseismic records generated by moderate and strong earthquakes occurring in oceans provide valuable waveform data. To utilize such data for structure studies, it is necessary to take into account of 3-D complexities at the source side. In many cases, source-side 3-D effects on teleseismograms are strong and coherent across many teleseismic stations. Some efforts have been made to exploit teleseismic waveforms to investigate slab structures (Silver & Chan 1986; Vidale *et al.* 1991; Zhan *et al.* 2014), but they have not been broadly applied, partly due to the difficulty of accurately modelling 3-D teleseismic wave propagation.

Understanding of source-side 3-D effects relies on reliable and efficient calculation of 3-D teleseismic synthetic waveforms. The Spectral Element Method (SEM) software package SPECFEM3D_GLOBE (Komatitsch & Tromp 1999, 2002; Tromp *et al.* 2008) and Finite Difference (FD) (Igel *et al.* 2002) method have been used in simulating 3-D global seismic wave propagation, but they are computationally costly for modelling high frequency waves at teleseismic distances. Moreover, FD methods usually have the problem of dealing with sharp interfaces (e.g. topography), and SPECFEM3D_GLOBE uses a stress equivalence to approximate a water layer and thus cannot simulate multiple phases in ocean water. To improve computational efficiency, we propose a hybrid method solution that uses a high-resolution 3-D simulation method (i.e. SEM) to compute complex wavefield in source region, and then propagates that wavefield to the remaining volume of the Earth by a 1-D method, i.e. Direct-Solution-Method (DSM). One of the previous hybrid methods was introduced by Okamoto (1993, 1994), in which a 2-D or 2.5-D FD method was combined with a plane wave input to compute teleseismic body waves. This method was applied to an earthquake near the Kuril trench (Okamoto 1994) and the 2006 M_w7.7 tsunami earthquake in Java (Okamoto & Takenaka 2009). In both cases strong 2-D/2.5-D source-side effects were observed and were better modelled by the hybrid approach. However, while a plane wave approximation may suffice for single seismic phases, such as direct *P*-wave, it would be problematic for multiple phases that have similar arrival times. As a receiver-side hybrid method, the SEM-DSM coupling developed by Monteiller *et al.* (2013) was successfully applied to 3-D receiver function analysis, in which plane wave approximation is not required and topography can be accurately handled at the receiver side. In general, a hybrid method can be implemented with any source and receiver configuration, including source-side, receiver-side or even mid-way coupling (Masson & Romanowicz 2017b). Here, we develop a similar SEM-DSM coupling implemented at the source-side to account for the 3-D structures. The previous version of our coupling code was based on SEM and the geometric ray theory and was only

able to compute teleseismic direct *P*-wave and direct *S*-wave (Meng *et al.* 2012; Zhan *et al.* 2012). Then the work of Monteiller *et al.* (2013) inspired us to replace the ray theory with DSM, which can accurately compute complete 1-D synthetic seismograms.

This paper is organized as follows. In Section 2, we use the representation theorem to justify our coupling theory and discuss the approximations made in the implementation. In Section 3, our hybrid method is validated via comparing hybrid synthetics with 1-D DSM and 3-D SEM synthetics. In Section 4, we discuss some issues in modelling including potential errors in numerical calculations and solutions. Finally, Section 5 contains two examples of subduction zone earthquakes, the 2016-10-27 M_w6.0 southern Chile offshore earthquake and the 2009-09-10 M_w5.9 Sea of Okhotsk earthquakes, which show the potential application of our hybrid method in teleseismic waveform modelling.

2 METHODS

Our hybrid method interfaces SEM (SPECFEM3D_Cartesian) running in a source region with DSM outside the source region to teleseismic distances. As a 1-D synthetic simulation tool, DSM has the advantage of high accuracy and fast speed (or fast convergence rate). As a 3-D wave propagation simulation tool, SEM can handle full 3-D velocity structures, topography, fluid/solid interfaces, and complex geometries accurately. Therefore, interfacing SPECFEM3D_Cartesian with DSM can substantially reduce computational cost while maintaining high accuracy of 3-D effects from source-side.

2.1 DSM and SEM

The SPECFEM3D_Cartesian package is best suited for modelling seismic wave propagation at local or regional scales (Komatitsch & Tromp 1999), and is widely used in the seismological community (Komatitsch 2004; Lee *et al.* 2009; Tape *et al.* 2009). Similar to Finite Element (FE) methods, SPECFEM3D_Cartesian solves the weak form of the seismic wave propagation equation and can therefore accurately handle traction-free surfaces and irregular internal discontinuities (elastic-elastic or acoustic-elastic). SPECFEM3D_Cartesian also allows for many types of seismic complexities, such as attenuation and anisotropy. It is more efficient than other 3-D FE methods. This is mainly due to the fact that the Legendre basis functions and Gauss–Lobatto–Legendre (GLL) quadrature used in SPECFEM3D_Cartesian can diagonalize the mass matrix, and therefore lead to higher convergence rates (Komatitsch & Tromp 1999). The 'localization property' of SEM makes it well-suited for parallel programming. Both MPI parallel programming and GPU accelerating (Komatitsch *et al.* 2009) have been implemented in SPECFEM3D_Cartesian.

Similar to SEM, DSM also solves the weak form of the wave equation (Geller & Ohminato 1994; Geller & Takeuchi 1995; Takeuchi *et al.* 1996; Kawai *et al.* 2006), but in the frequency domain. And vector spherical harmonics are used to decompose displacement field. The displacement for each frequency is represented as,

$$\mathbf{u}(r,\theta,\phi) = \sum_{lm} U^{lm}(r)\mathbf{S}^{lm1}(\theta,\phi) + V^{lm}(r)\mathbf{S}^{lm2}(\theta,\phi) + W^{lm}(r)\mathbf{T}^{lm}(\theta,\phi). \tag{1}$$

Here, $\mathbf{u}$ is the displacement field and r, θ and ϕ are spherical coordinates. $\mathbf{S}^{lm1}$ is the vector spherical harmonic that corresponds to $\mathbf{S}^{1}_{lm}$ in Kawai *et al.* (2006), where we switch to a superscript notation to avoid confusion with Cartesian vector components, which will be used later. Similarly, $\mathbf{S}^{lm2}$ and $\mathbf{T}^{lm}$ are the other two vector spherical harmonics and correspond to $\mathbf{S}^{2}_{lm}$ and $\mathbf{T}_{lm}$ in Kawai *et al.* (2006) respectively. l is an angular order and m is an azimuthal order. The radial functions are expressed as

$$U^{lm}(r) = \sum_{k} c^{lmk1} X^{k}(r) \tag{2}$$

$$V^{lm}(r) = \sum_{k} c^{lmk2} X^{k}(r) \tag{3}$$

$$W^{lm}(r) = \sum_{k} c^{lmk3} X^{k}(r). \tag{4}$$

The function $X^k(r)$ is composed of a number of linear spline functions and the superscript k denotes the index of radial nodes (Kawai *et al.* 2006). The unknown parameters in eqs (2)–(4) are the coefficients c^{lmk1}, c^{lmk2} and c^{lmk3}, which can be derived from solving a system of linear equations. The spherical harmonic decomposition simplifies the problem significantly and decouples spheroidal and toroidal modes at teleseismic distances, similar to the normal mode theory for a spherically symmetric Earth model. However, instead of computing the eigenvalue-eigenfunctions of each individual mode, DSM specifies the time length of synthetics and the number of frequencies, thus avoiding the problem of missing overtones and allowing it to work effectively even at high frequencies. For example, Kawai *et al.* (2006) computed global synthetic waveforms up to 2 Hz using only a few CPU processors. DSM is capable of handling transverse isotropy (TI) and attenuation. Self-gravitation and the Coriolis force are currently not taken into account in DSM, which could lead to a maximum error of a few per cent for long period waves in some cases (Komatitsch & Tromp 2002). However, DSM synthetics are usually sufficiently accurate for teleseismic body-wave analysis.

In order to couple SEM with DSM, we need to compute Green's functions for three independent single force excitations, which are summarized in the Appendix. Another technical issue is the slow convergence rate of the right hand side of eq. (1) when target receiver depths are close to source depth. By analysing the Green's function of the scalar Helmholtz equation and DSM solutions for single force excitation, we find that the teleseismic displacement and stress solutions near source depth oscillate around their true values. Thus, our solution takes an average value over some integer periods of the oscillation to suppress the oscillation effect and therefore improve computational efficiency (see supplementary material)

2.2 Coupling theory

Hybrid seismic simulation methods can be generally classified into receiver-side coupling, source-side coupling, and mid-way coupling. In a pioneering work, Alterman & Karal (1968) combined 1-D solutions in a homogeneous full-space with FD simulation to study the problem of seismic wave propagation in a layered half-space. This is often referred as AK-type receiver-side interfacing, and was improved by numerous later studies (see e.g. Bielak & Christiano 1984; Fäh *et al.* 1994; Zahradník & Moczo 1996; Robertsson & Chapman 2000; Bielak *et al.* 2003; Yoshimura *et al.* 2003; Opršal *et al.* 2009; Monteiller *et al.* 2013; Baker & Roecker 2014; Tong *et al.* 2014a,b; Borisov *et al.* 2015; Monteiller *et al.* 2015; Wang *et al.* 2016; Masson & Romanowicz 2017a,b; Beller *et al.* 2018; Clouzet *et al.* 2018). Similarly, source-side coupling enables investigation of complex structure effects near seismic events, but only a few attempts have been reported (Okamoto 1993, 1994). Okamoto (1993) used the reciprocity principle to switch the roles of source and receiver, and turned the problem of source-side coupling into one of receiver-side coupling. Mid-way hybrid methods are a combination of both source- and receiver-side coupling and therefore more difficult than either. Consequently, even fewer studies have exploited hybrid methods to analyse heterogeneities far from source and receivers (Wen & Helmberger 1998), although recent synthetic tests show its promising potential in deep Earth tomography (Masson & Romanowicz 2017a,b).

Here we utilize the representation theorem to derive the equation for SEM-DSM source-side coupling. First, we review the representation theorem in seismology, which is described well in the Chapter 2 of Aki & Richards (2002). Suppose that $\mathbf{u}(\mathbf{x}, t)$ is a displacement field defined in a model $\mathscr{V}_1$ and another displacement field $\mathbf{G}(\boldsymbol{\xi}, t)$ is defined in a different model $\mathscr{V}_2$ (Fig. 2a). Here, $\mathscr{V}_i$ is a model, by which we mean a portion of physical space V_i endowed with certain properties, e.g. seismic velocity and density structures. Both $\mathbf{u}(\mathbf{x}, t)$ and $\mathbf{G}(\boldsymbol{\xi}, t)$ satisfy the elastodynamic equation and are determined by their corresponding body forces and boundary conditions. For the portion of the field $\mathbf{u}(\mathbf{x}, t)$, in the submodel $\mathscr{V}_3$ shared by $\mathscr{V}_1$ and $\mathscr{V}_2$, the representation theorem gives (see eq. 2.41 in Aki & Richards 2002)

$$u_n(\mathbf{x}, t) = \int_{-\infty}^{\infty} d\tau \int_{V_3} f_i(\boldsymbol{\xi}, \tau) G_{in}(\boldsymbol{\xi}, t-\tau; \mathbf{x}, 0) dV(\boldsymbol{\xi}) + \int_{-\infty}^{\infty} d\tau \int_S [T_i(\boldsymbol{u}(\boldsymbol{\xi}, \tau), \mathbf{n}) G_{in}(\boldsymbol{\xi}, t-\tau; \mathbf{x}, 0) - u_i(\boldsymbol{\xi}, \tau) c_{ijkl}(\boldsymbol{\xi}) n_j \frac{\partial G_{kn}}{\partial \xi_l}(\boldsymbol{\xi}, t-\tau; \mathbf{x}, 0)] dS(\boldsymbol{\xi}), \quad \mathbf{x} \subset V_3 \tag{5}$$

where $S(\boldsymbol{\xi})$ is the boundary of physical space V_3 and the Einstein summation convention is adopted.

Here, $f_i(\boldsymbol{\xi}, \tau)$ represents a body force and $T_i(\boldsymbol{u}(\boldsymbol{\xi}, \tau), \mathbf{n})$ is traction associated with $\mathbf{u}(\boldsymbol{\xi}, \tau)$ and a surface normal vector $\mathbf{n}$. The Green's function $G_{in}(\boldsymbol{\xi}, t-\tau; \mathbf{x}, 0)$ denotes the ith component of $\mathbf{G}(\boldsymbol{\xi}, t-\tau)$ due to an impulsive force in the n-direction applied at $\mathbf{x}$ and time zero, and $c_{ijkl}(\boldsymbol{\xi})$ is elastic modulus and $c_{ijkl}(\boldsymbol{\xi}) n_j \frac{\partial G_{kn}}{\partial \xi_l}(\boldsymbol{\xi}, t-\tau; \mathbf{x}, 0)$ as a whole is traction associated with G_{kn}.

We note that the models $\mathscr{V}_1$ and $\mathscr{V}_2$ must have exactly the same seismic properties and physical space in the shared portion $\mathscr{V}_3$. However, the representation theorem does not impose any restriction on that in the non-shared portion $\mathscr{V}_2 - \mathscr{V}_3$ and $\mathscr{V}_1 - \mathscr{V}_3$. In other words, seismic properties and/or physical space in the non-shared portion could be different. This feature of representation theorem has been skilfully used in solving elastodynamic problems with a slipped fault (see Chapter 3 of Aki & Richards 2002), in which another displacement field $\mathbf{G}$ defined in a model without the fault is introduced to circumvent the problem of discontinuous slip and strain on the fault.

Similarly, we use this feature of the representation theorem in our SEM-DSM hybrid method. Specifically, the model $\mathscr{V}_2$ is a simple 1-D layered Earth model while the $\mathscr{V}_1$ corresponds to another different Earth model with local 3-D complex seismic structures and/or topography near the source (Fig. 2b). $\mathscr{V}_1$ and $\mathscr{V}_2$ have a shared portion $\mathscr{V}_3$, which represents the vast majority of the two Earth models excluding the source region. Both $\mathscr{V}_1$ and $\mathscr{V}_2$ have the same physical space and 1-D seismic structure in this shared $\mathscr{V}_3$. For the source region, $\mathscr{V}_1$ and $\mathscr{V}_2$ could have different physical spaces and/or seismic properties. For example, topography, ocean water and/or a subducted slab are allowed in the model $\mathscr{V}_1$ while the model $\mathscr{V}_2$ has a 1-D seismic structure and no topography. Then, we can use eq. (5) to compute teleseismic synthetic seismogram u_n associated with the 3-D model $\mathscr{V}_1$.

In eq. (5), the displacement Green's function $\mathbf{G}$ and its associated stress or strain are straightforwardly computed by using the DSM. However, the exact 3-D wavefield $u_i(\boldsymbol{\xi}, \tau)$ and $T_i(\boldsymbol{u}(\boldsymbol{\xi}, \tau), \mathbf{n})$ on the right hand side of eq. (5) can only be obtained by solving the equation of wave propagation in the entire physical space of Earth V_1. Thus, eq. (5) alone cannot reduce computation cost. We need to make the following approximations and limit the SEM simulation from V_1 to the much smaller physical space $V_1 - V_3$, the source region:

$$u_i(\boldsymbol{\xi}, \tau) \text{ from global 3-D simulation} \approx u_i(\boldsymbol{\xi}, \tau) \text{ from local 3-D simulation} \tag{6}$$

$$T_i(\boldsymbol{u}(\boldsymbol{\xi}, \tau), \mathbf{n}) \text{ from global 3-D simulation} \approx T_i(\boldsymbol{u}(\boldsymbol{\xi}, \tau), \mathbf{n}) \text{ from local 3-D simulation} \tag{7}$$

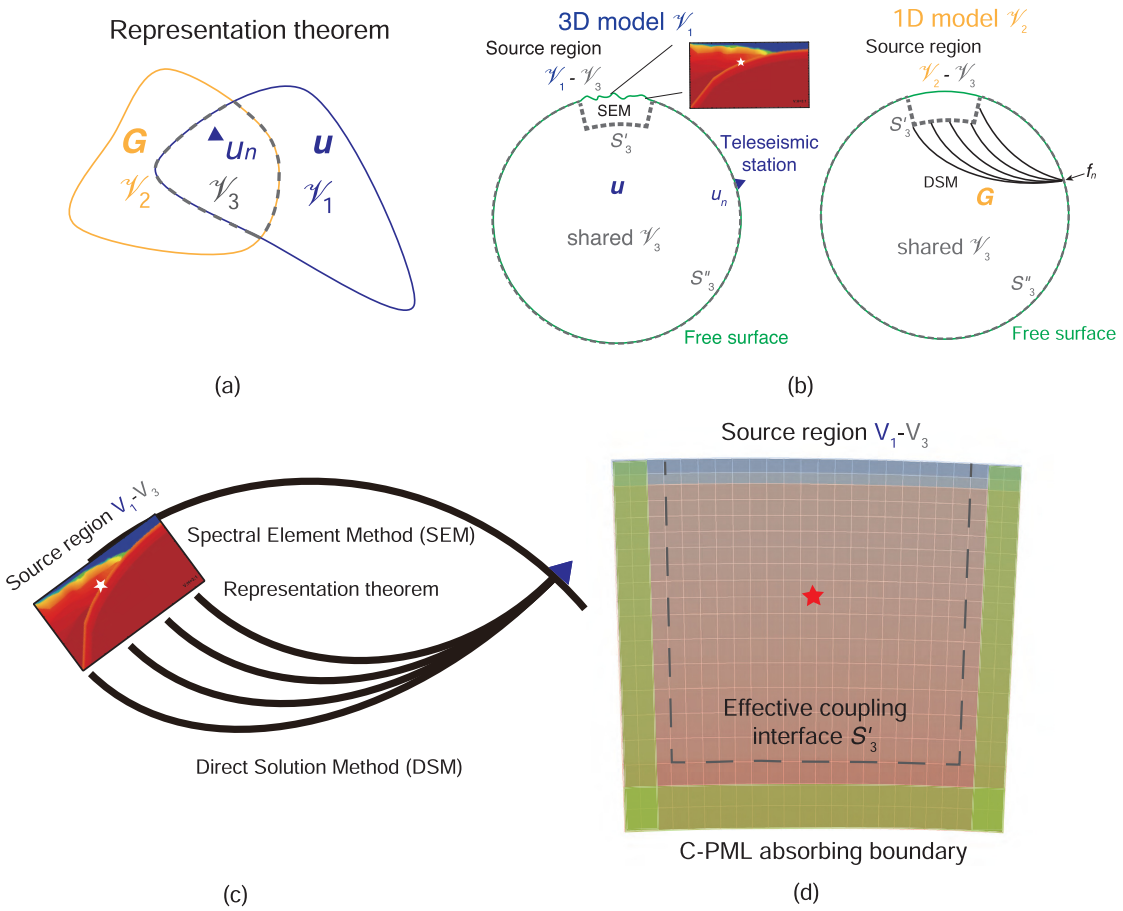

Figure 2. Schematic figure of the representation theorem and coupling scheme. (a) Models $\mathscr{V}_1$, $\mathscr{V}_2$ and $\mathscr{V}_3$ and their associated displacement fields **G** and **u** in the context of the representation theorem. The submodel $\mathscr{V}_3$ is shared by $\mathscr{V}_1$ and $\mathscr{V}_2$. u_n in eq. (5) is the portion of **u** in V_3, which is the physical space of model $\mathscr{V}_3$. The grey dashed line represents the boundary of V_3. (b) The mapping of (a) in our hybrid method. $\mathscr{V}_2$ is a 1-D Earth model and we use DSM to compute the Green's function **G**. $\mathscr{V}_1$ is another Earth model, in which free surface topography and 3-D velocity structures (e.g. subducted slab shown in the inset figure) are allowed in the source region $\mathscr{V}_1 - \mathscr{V}_3$. S_3' (thick grey dashed line) and S_3'' (thin grey dashed line) together are the boundary of V_3. (c) Schematic cartoon to illustrate the configuration of SEM-DSM coupling. (d) Mesh and configuration of a source-side SEM box. This box is equivalent to $\mathscr{V}_1 - \mathscr{V}_3$ in (a) and (b). The light green bands represent C-PML absorbing boundaries and the coupling interface (grey dashed line) are implemented inside the C-PML layers.

where 'local 3-D simulation' means running SEM in the source-side physical space $V_1 - V_3$ endowed with 3-D seismic properties (Figs 2b and c).

For the local 3-D simulation, absorbing boundary conditions, such as Convolutional Perfectly Matched Layer (C-PML), are applied on the four sides and the bottom of SEM box (Fig. 2d) and the top boundary is free surface. Thus, eq. (5) is exactly accurate, but truncating the global model and applying absorbing boundary conditions bring in some errors, due to the differences between the left- and right-hand side of eqs (6) and (7). This issue have been thoroughly discussed in previous relevant literature (e.g. van Manen *et al.* 2007; Masson & Romanowicz 2017b). In our source-side coupling, these approximations mean that seismic waves exiting and then reentering the SEM box cannot be accounted for. In most instances, those waves are either beyond the time window of interest, or too small due to inelastic attenuation and/or geometric spreading, so approximations in eqs (6) and (7) are usually valid. An example of errors caused by these approximations and some seismic phases with possibly large errors are discussed in the next section.

Because the body force term in eq. (5) does not exist in our hybrid scheme, we can rewrite eq. (5) as

$$u_n^{\text{hybrid}}(\mathbf{x}, t) = \int_{-\infty}^{\infty} \mathrm{d}\tau \int_S [T_i^{\text{SEM}}(\boldsymbol{u}(\boldsymbol{\xi}, \tau), \mathbf{n}) G_{in}^{\text{DSM}}(\boldsymbol{\xi}, t-\tau; \mathbf{x}, 0) - u_i^{\text{SEM}}(\boldsymbol{\xi}, \tau) c_{ijkl}(\boldsymbol{\xi}) n_j \frac{\partial G_{kn}^{\text{DSM}}}{\partial \xi_l}(\boldsymbol{\xi}, t-\tau; \mathbf{x}, 0)] \mathrm{d}S(\boldsymbol{\xi}), \tag{8}$$

where '$*$' denotes convolution. In the frequency domain, it is

$$u_n^{\text{hybrid}}(\mathbf{x}, \omega) = \int_S [T_i^{\text{SEM}}(\boldsymbol{u}(\boldsymbol{\xi}, \omega), \mathbf{n}) G_{in}^{\text{DSM}}(\boldsymbol{\xi}, \omega; \mathbf{x}, 0) - u_i^{\text{SEM}}(\boldsymbol{\xi}, \omega) c_{ijkl}(\boldsymbol{\xi}) n_j \frac{\partial G_{kn}^{\text{DSM}}}{\partial \xi_l}(\boldsymbol{\xi}, \omega; \mathbf{x}, 0)] \mathrm{d}S(\boldsymbol{\xi}). \tag{9}$$

The surface S is defined as the boundary of the shared physical space V_3, which corresponds to the coupling interface within the SEM box (thick grey dashed line S_3' in Fig. 2b) and most of the Earth's free surface (thin grey dashed line S_3'' in Fig. 2b). Because the free surface is traction free, where both tractions $T_i^{\text{SEM}}(\boldsymbol{u}(\boldsymbol{\xi}, \omega), \mathbf{n})$ and $c_{ijkl}(\boldsymbol{\xi}) n_j \frac{\partial G_{kn}^{\text{DSM}}}{\partial \xi_l}(\boldsymbol{\xi}, \omega; \mathbf{x}, 0)$ are zero, the effective part of S is just the coupling interface S_3' (Figs 2b and d).

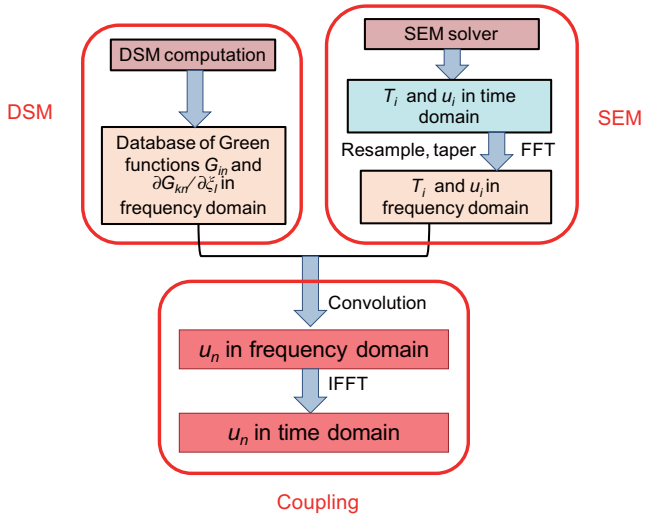

Figure 3. The work flow of the SEM-DSM hybrid method.

In summary, the representation theorem serves as a bridge to connect SEM with DSM, and eqs (6) and (7) help reduce computational cost. Note that this coupling theorem can naturally be extended to handle mid-way coupling, in which the representation theorem must be applied twice to inject a global wavefield into the target region and then again to project the local 3-D wavefield back into the global background model (Masson & Romanowicz 2017a,b).

2.3 Implementation

The workflow of our SEM-DSM hybrid method is composed of DSM simulation, SEM computation, and a final step of coupling (Fig. 3). Following the idea of modular programming, we decompose the workflow into these three parts and implement them independently.

We first run DSM in the frequency domain to compute Green's function database associated with the three single forces and store them on a hard drive. Depending on specific time length of output synthetics and maximum frequency resolved, DSM discretizes frequency domain solutions into a finite number of frequency bands and computes the solutions for all frequencies in parallel. Because DSM runs in a spherical coordinate system, the Green's function database consists of a number of displacement and strain synthetics at a range of given spatial locations, parameterized as azimuth, depth (or radius) and distance, for each particular frequency. We fix the azimuth parameter at zero, because there is no azimuthal dependence for a vertical single force excitation and all the non-zero azimuth Green's functions for the two horizontal single forces can be easily expressed as a linear combination of their zero-azimuth synthetics. The depth information directly comes from the local SEM model parameterization and the distance table is a linearly spaced array with a given range, based on which we use a Lagrange interpolation scheme to generate accurate synthetics at target distances (more details in Section 3). Computing DSM displacement is straightforward and we follow the example of Monteiller *et al.* (2013) to compute the strain. Other technique details such as vertical gridding space and artificial attenuation can be found in the literature (e.g., Geller & Ohminato 1994; Kawai *et al.* 2006).

The second step involves model creation and running the SEM solver. To be consistent with the spherical coordinates used in DSM, we adopt the cubed sphere coordinates in SEM meshing. This offers an additional advantage of reserving the curvature of the free surface and other internal discontinuities. The SEM model parameterization in the coupling method is almost the same as normal (un-coupled) SEM simulations. However, the incorporated 3-D model needs to gradually transit to match the 1-D background model at the coupling interface, because the representation theorem requires the same seismic properties in the SEM and DSM models on the coupling interface. Schemes of an appropriate 3-D-1-D structure transition (see the slab multipathing example in Section 4.2) or the consequences of mismatch (see the shallow thrust earthquake example in Section 4.1) must be carefully considered.

The local SEM box is a truncated version of a global model and requires absorbing conditions on its four sides and bottom boundary. SPECFEM3D_Cartesian provides two options for an absorbing boundary: Stacey or Complex-Frequency-Shifted Unsplit-field Perfectly Matched Layer (CFS-UPML, a special type of C-PML absorbing boundary) absorbing boundary. The CFS-UPML option is strongly recommended here, due to its much better performance (Xie *et al.* 2014), despite its additional computation cost.

When running the SEM solver, both displacement and stress on the coupling GLL points are simultaneously computed and stored. At the same time, depths of those interfacing points across all the CPUs are collected to build a depth table, whose Green's functions are computed through DSM. In order to avoid an incomplete wavefield, we set a sufficiently long time window length to run the SEM solver.

In the final step of coupling, SEM synthetic waveforms are convolved with DSM Green's functions. To accelerate the computation, we resample SEM synthetics with a proper sampling rate and compute the FFT to transform them into the frequency domain. Then, the convolutions of eq. (9) can be easily carried out in the frequency domain and an IFFT is applied to the frequency domain synthetics to obtain the time domain solutions.

3 VALIDATION

In this section, we begin with validation of the hybrid method using a 1-D-model benchmark test, and then proceed to further confirm by comparing hybrid synthetics with 'exact' results from full 3-D SEM simulations. Finally, some numerical issues and solutions are discussed in Section 3.3.

3.1 1-D benchmark of teleseismic phases

Some commonly used teleseismic phases, including P, Pdiff, PcP, PP, PKP, PKiKP, Rayleigh, Love, S, ScS, SKS and SKKS, are benchmarked against DSM synthetics here. We create an SEM box with dimensions of 2° (Longitude) × 2° (Latitude) × 100 km (depth) and within the box impose a normal fault earthquake with a half-duration of 0.5 s. The earthquake is horizontally located at the centre of the SEM domain at a depth of 25 km. The IASP91 model (including attenuation) (Kennett & Engdahl 1991) is used as the 1-D background model here and all other examples in this paper. The number of elements is 128 × 128 × 49, which allows us to resolve a minimum period of 0.74 s. We apply a 9 km thick C-PML absorbing layer on the bottom boundary and 0.07° (roughly 7.8 km) thick layers on each of the four sides. We set the time step to 0.015 s and the number of time steps to 12000 for a time length of 180 s. Such a long time length ensures that most seismic energy is ultimately absorbed well by the C-PML layers. The SEM simulation took about 5 hr on 64 processor cores. Fig. 4 shows the benchmark results where the hybrid synthetics agree well with the DSM results. We note that the PnPn phase is clear in the synthetics (Fig. 4b), that is not common in real data. This might be due to the low attenuation of the crust and top mantle, and an oversimplified Moho discontinuity in the IASP91 model. Nevertheless, PnPn is a good example to illustrate some numerical difficulties inherent in our hybrid method, as we will discuss in Section 3.3.

3.2 3-D synthetics benchmark

In realistic cases, an ocean water layer, sediment basin, and topography/bathymetry might have very strong 3-D source-side effects. We would expect similar effects of sediment basin and a water layer in generating teleseismic waveform complexities, since both of them have zero or very low shear velocity. We test the water and topography effects separately by benchmarking the hybrid synthetics against the synthetics generated from SEM simulations alone.

In Fig. 5(a), a model of a sinusoidal shaped free surface topography with a lateral dimension of 1° and a peak height of 10 km is tested. We set an explosive source with a duration of 6 s at a depth of 35 km below the topography peak. We create a chunk with sufficiently large dimensions of 44.8° (longitude) × 22.4° (latitude) × 2000 km (depth) (the lower panel in Fig. 5a) and run SEM to obtain the 'exact' solutions. The number of elements is 448 (longitude) × 224 (latitude) × 142 (depth) and the minimum resolved period is 5.6 s. We carefully choose the size of the chunk and locations of the source and receivers so that all the artificial boundary reflected/refracted waves arrive later than the benchmark time window (Fig. 5b). This ensures that the simulations are free of any artefacts from the boundaries. We then choose a smaller chunk surrounding the source (the upper panel in Fig. 5a) and apply our hybrid method to compute the synthetics. The hybrid synthetics (red lines in Fig. 5b) are almost identical with the 'exact' solutions (blue dashed lines in Fig. 5b). For comparison, we also compute the synthetics with no topography model (green lines in Fig. 5b). The topography has no visible effect on the direct *P*-waves, but distorts the depth phase pP significantly. The pP arrivals are delayed and their amplitudes are increased due to the focusing effects. The time length of the full 3-D SEM simulation with the large chunk is 894 s and the computation took about 5 hr using 512 processor cores. In contrast, Our hybrid method only took about 10 minutes using 10 CPUs to complete the SEM simulation in the much smaller source-side box. This translates to a reduction of computational cost by more than three orders of magnitude.

Next, effects of water layer are tested in a similar way by replacement of the topography by a 10 km thick water lake (Fig. 6a). Because the *P*-wave velocity of water is much lower than that of the upper crust, the resolved minimum period is 9.3 s, which is longer than the 5.6 s in the previous pure topography case. Thus, we specify a source duration of 10 s here. Fig. 6(b) shows that the hybrid synthetics (red lines) also agree well with the 'exact' solution (blue dashed lines). As compared with the 1-D synthetics, the effects of water reverberations and scattering are strong enough to clearly distort the waveforms even at periods greater than 9.3 s, when depth phase pP and water phase pwP mix. At shorter periods, the water reverberations can be more clearly identified on waveforms recorded by a dense array (Stewart & Helmberger 1981; Chu *et al.* 2011).

3.3 Numerical difficulties and solutions

In this subsection we discuss a few numerical difficulties during the implementation and the error caused by the local SEM approximations in eqs (6) and (7).

As mentioned in Section 2.3, the DSM Green's function database is composed of a large number of 1-D synthetics for interfacing points. We first collect the depth information of the interfacing points to form a depth table and generate an evenly spaced distance table. Then the Green's functions for all the locations are computed by pairing each depth and distance in the two tables. Finally, we use 16-degree Lagrange polynomial interpolation to calculate the Green's functions at target distances.

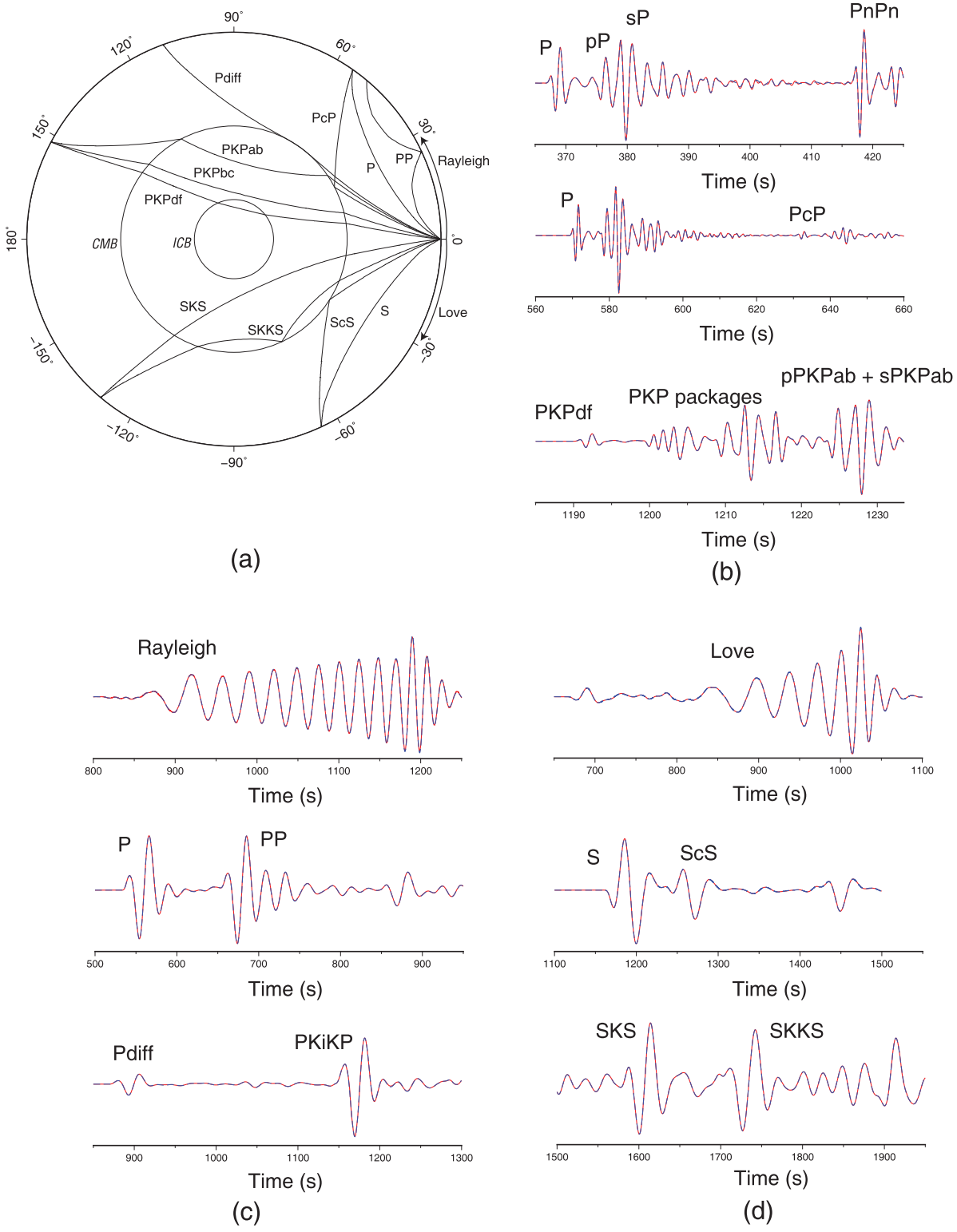

Figure 4. 1-D teleseismic phases benchmark. The source is a normal fault earthquake (strike = 0°, dip = 90° and rake = −90°) and all the synthetics are on the azimuth of 30°. The blue dashed lines are DSM synthetics and the red lines show hybrid synthetics. (a) Ray paths of teleseismic phases in (b)–(d). (b) Short period vertical displacement. A band-pass filter 0.4–1.2 Hz is applied to the synthetics. The distance from top to bottom are 30°, 55° and 155°. (c) Long period vertical displacement. A band-pass filter 0.01–0.05 Hz is applied. The distance from top to bottom are 30°, 50° and 110°. (d) Long period transpose (the top two panels) and radial (the bottom panel) displacement. A band-pass filter 0.01–0.05 Hz is applied. The distance from top to bottom are 30°, 65° and 130°.

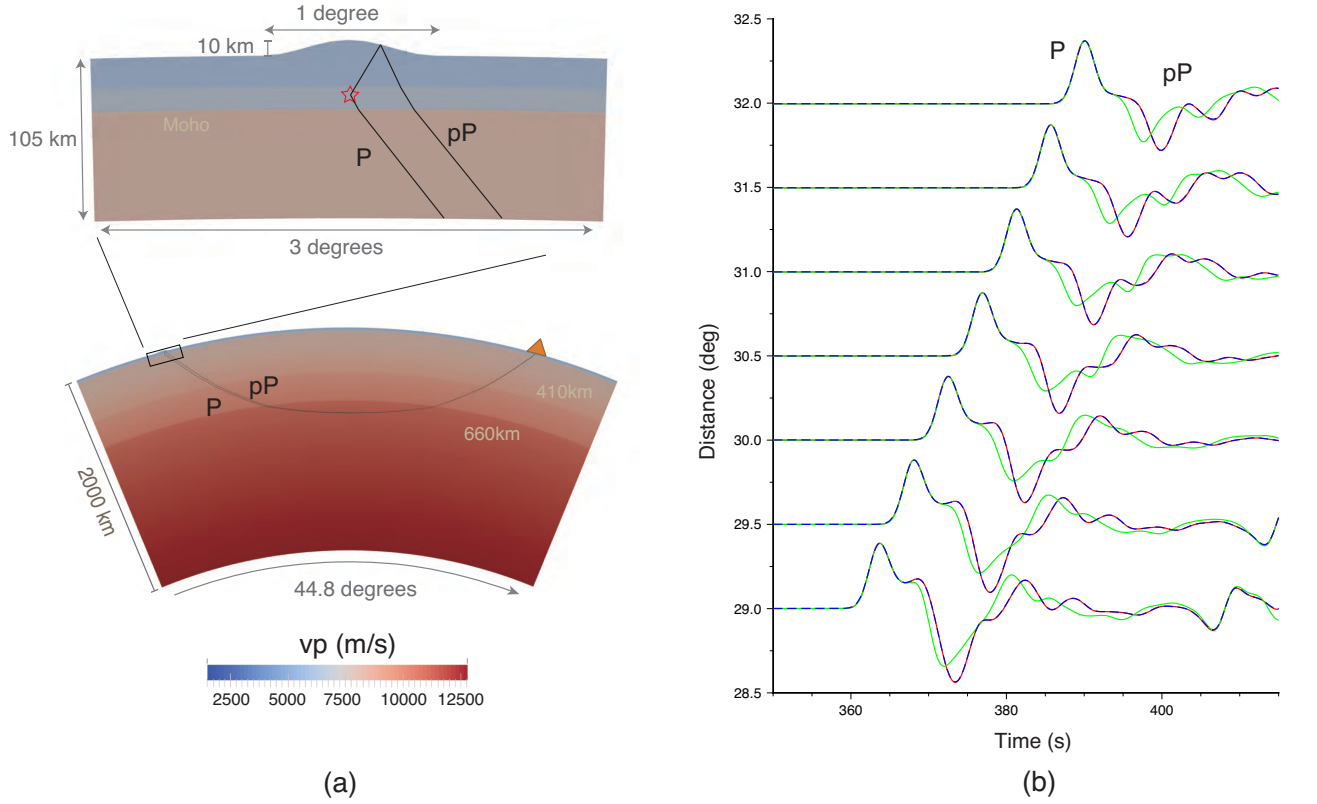

Figure 5. Benchmark of a 3-D topography model. (a) Models of full SEM simulation (the bottom panel) and hybrid computation (the upper panel). The dimensions of the full SEM simulation are 44.8° (radial direction) × 22.4° (transpose direction) × 2000 km (vertical direction). The SEM box in the hybrid method has dimensions 3° × 3° × 105 km. (b) Distance profile of synthetics. The red lines are hybrid synthetics and the blue dashed lines show synthetics through the full SEM simulation. For comparison, the 1-D synthetics without topography effects are plotted as green lines.

We note that a proper space of distance table is critical for high quality of Lagrange interpolation (see Supporting Information Figs S6 and S7). We take the top seismogram in Fig. 4(b) as an example to show the effects of distance interval on accuracy of synthetics. Fig. 7 shows the results for four different distance intervals of 0.1°, 0.05°, 0.03° and 0.01°. In general, smaller distance interval results in more accurate synthetics. Specifically, the choice of a proper distance interval depends on the slowness of the seismic phase being studied. For example, the errors corresponding to phase PnPn are larger than that of the direct *P*-waves for the same distance interval, due to the larger slowness of PnPn. Here, the frequency band in Fig. 7 is 0.4–1.2 Hz and the slowness of the direct *P*-wave is about 8.85 s/deg. The distance interval should be adjusted accordingly for a different frequency band and/or slowness. This issue has also been discussed by Fuji *et al.* (2012) and they proposed a method of move-out correction, by which accurate interpolations can be achieved even using a rather large distance spacing. If only one or a few phases are of concern and their slownesses are known, the move-out correction might allow us to use a large distance spacing and therefore save storage volume.

In Fig. 7(d), we observe some errors between sP and PnPn. Although this level of error is low and usually can be neglected for practical purposes, it would be helpful to resolve the origin of these errors. Fig. 8 shows the results of a high spatial resolution coupling case, in which a total number of 25 GLL points on one coupling face are used to couple with 1-D Green's functions, instead of only one as in the case of the low spatial resolution mode (Fig. 7d). In practice, a coupling face is discretized with a number of GLL points (e.g. 25 points in Fig. 8a) and each GLL point has its own coupling parameters, including normal vector, Jacobian, displacement, and stress. The contribution from each GLL point is summed up to form the surface integral of eq. (9). In contrast, the low spatial resolution mode only uses the information of the central point, whose Jacobian is the summation of the 25 sub-Jacobians. As expected, finer discretization results in smaller error of *P*-wave coda than that in Fig. 7(d). Although this improvement of fitting is relatively small in this case, it might be important for coarse mesh grid simulations or scattering wave analysis, which usually focuses on signals with small amplitudes. We note that the Gauss-Lobatto-Legendre quadratures used in SPECFEM3D_Cartesian greatly facilitate implementation of the SEM-DSM source-side coupling. Using these quadratures in SEM offers a number of advantages, such as high accuracy of discretizing and diagonal mass matrix. Some of these advantages are inherited in our hybrid method. For example, the GLL quadratures significantly simplify the discretization of the surface integrals in the coupling eq. (9) and their high quality is important for an accurate discretization. More details about this can be found in Masson *et al.* (2014).

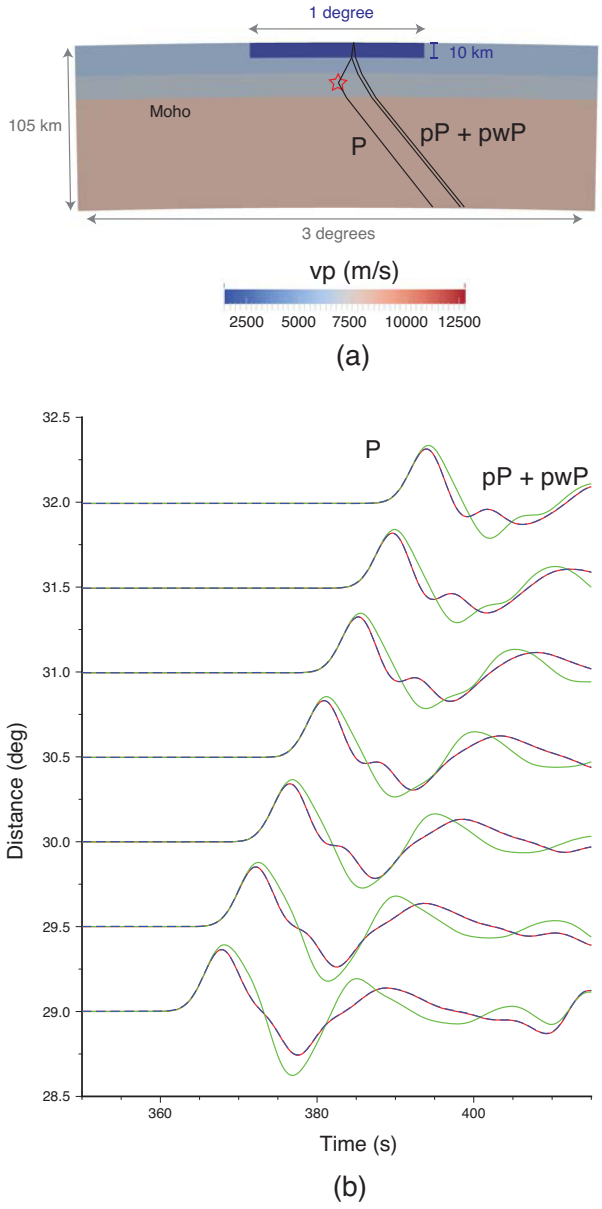

Figure 6. Benchmark of a water lake model. (a) A model of water lake. The dark blue area shows a water lake. The red star is an explosion source at a depth of 20 km. (b) The red lines are hybrid synthetics and the blue dashed lines show synthetics through the full SEM simulation. For comparison, the 1-D synthetics without the effects of water lake are plotted as green lines. The dimensions of the full SEM simulation are the same as the lower panel in Fig. 5(a).

Another type of error comes from the approximations in eqs (6) and (7). Because of the model truncation, waves traveling from outside into the source-side SEM box are not taken into account in our hybrid method. Those seismic phases include multiple surface waves (such as R3, R4 and so on), reflected waves from the internal Earth discontinuities (e.g. near-source PcP and ScS), etc. For example, Fig. 9 shows an example of Moho reflected signals on the teleseismic seismograms. We compare synthetics for two models and analyse the error due to neglecting PmpP wave (and its reverberations in the crust). The first model of SEM box (the bottom panel of Fig. 9a) is exactly the same as the top panel of Fig. 5(a), which includes the Moho discontinuity. We then truncate this model at the depth of the Moho discontinuity to form another SEM box (the top panel of Fig. 9a). Because the Moho discontinuity is not fully implemented in the latter model, the C-PML layer absorbs the seismic waves traveling downwards to the bottom boundary and therefore PmpP cannot be produced. In Fig. 9(b), we can observe that the direct *P*-waves for the two models are consistent with each other, but some mismatches do appear at the arrival of the PmpP phase. It is therefore important to include the SEM domain Moho discontinuity, and other important discontinuities or sharp boundaries, which may cause multiple wave reflections and conversions. Depending on specific application, other potential boundaries could include a slab interface or a sediment basement, etc.

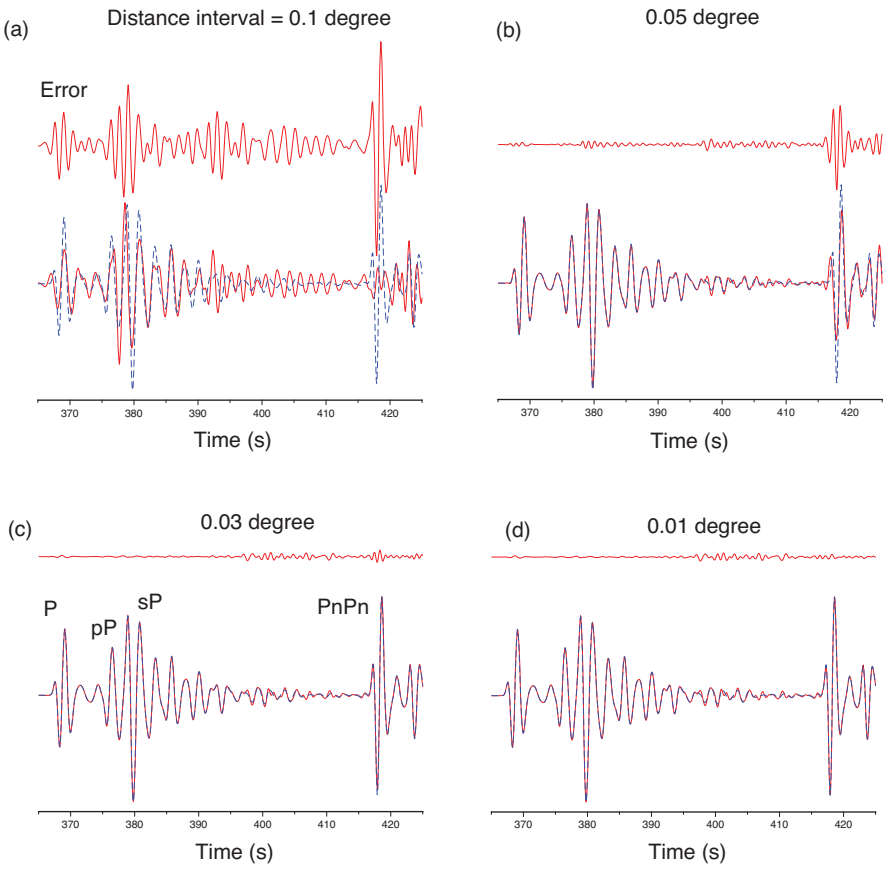

Figure 7. Errors corresponding to different distance spaces used in generating Green's function database. All the blue dashed lines here are the DSM synthetics at the distance of 30°, the same as the top one in Fig. 5(b). Four distance spaces 0.1°, 0.05°, 0.03° and 0.01° are tested. The bottom red line in each panel shows the hybrid synthetic. The top red line in each panel indicates the error, which is the discrepancy between the below blue dashed line and red line in the lower panel.

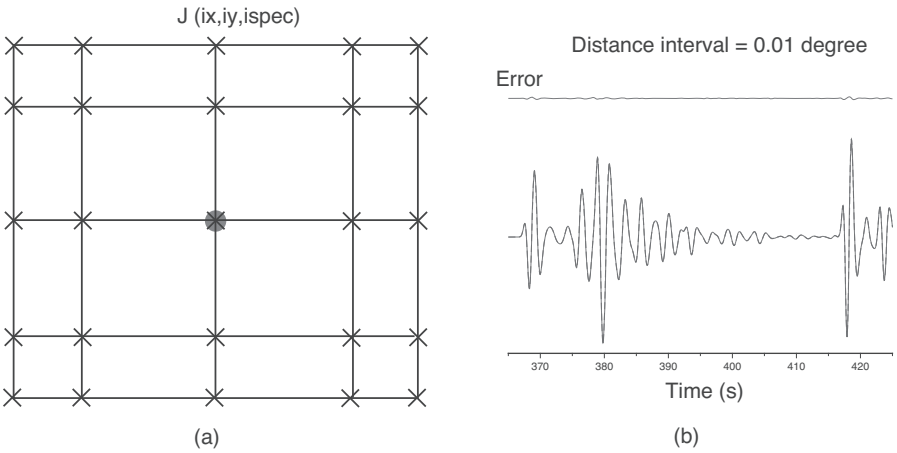

Figure 8. The 25 GLL points on a coupling face and synthetic. (a) Schematic cartoon to show the 25 GLL points on a coupling face. Each GLL point has its own Jacobian $J(ix, iy, ispec)$. Instead of using the central GLL point (grey circle) in a low spatial resolution coupling mode, all the GLL points (the 25 cross marks in this case) on the coupling face are involved in a high spacial resolution coupling mode. (b) Synthetic (red line in the lower panel) and error (red line in the upper panel) for the high spatial resolution coupling mode. This figure is the same as Fig. 7(d), but for high spatial resolution coupling mode. Comparing with Fig. 7(d), the error in the time window of 395–410 s is reduced, due to the finer spacial discretization of the coupling face.

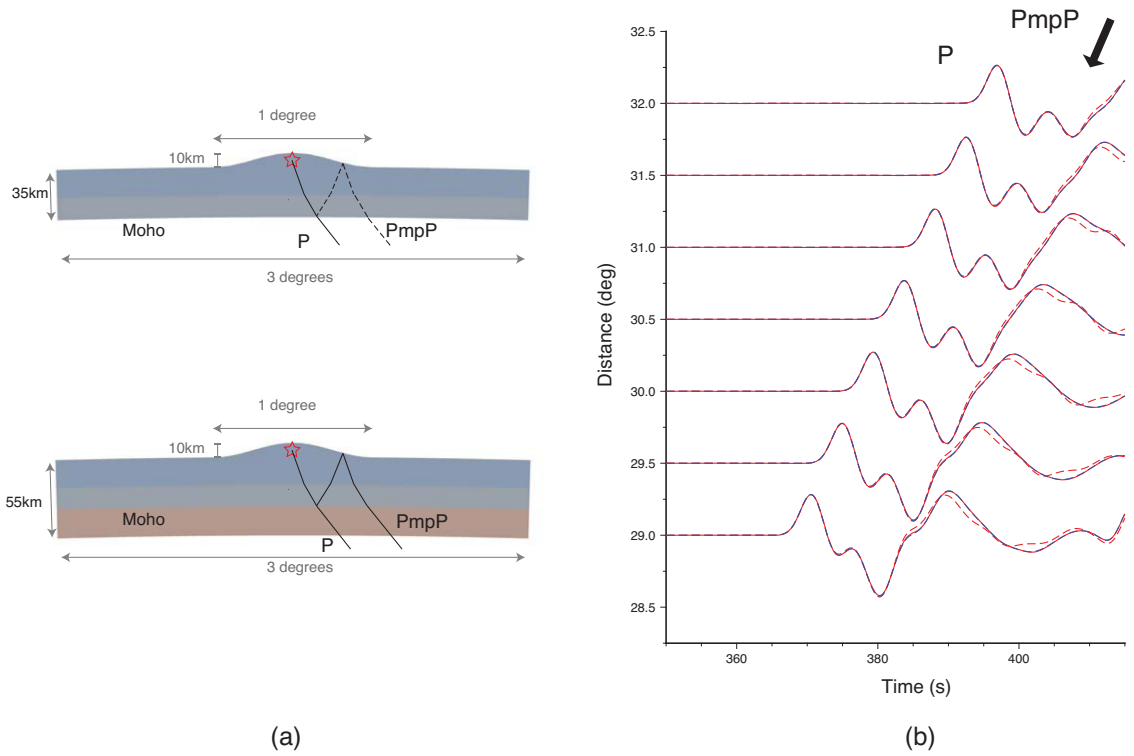

Figure 9. Testing the effect of neglecting refection wave PmpP, due to the truncation of the SEM box. (a) SEM boxes including the Moho discontinuity (the lower panel) and truncated at the Moho discontinuity (the upper panel). (b) Synthetics. The blue dashed lines are the 'exact' solution, from the full SEM simulation. The red lines are hybrid synthetics corresponding to the lower panel model in (a). The red dashed lines are associated with the upper panel model in (a). Because of the truncated Moho discontinuity, the signal PmpP, *P*-waves reflected on the Moho, back up to the free surface and then reflected to the station, are failed to be correctly computed in the red dashed lines.

Table 1. Part parameters of the GCMT solutions of the earthquakes #161027 and #090910. GCMT solutions provide two conjugate fault planes and the dip1 represents the more likely dip angles of the real fault planes, if we suppose that those two events are intraplate earthquakes.

Event ID	Date	Time	Latitude (°)	Longitude (°)	Depth (km)	M_w	dip1	dip2
#161027	10/27/2016	20:33:02	-33.83	-72.75	12.0	6.0	17	73
#090910	09/10/2009	02:46:55	48.20	154.68	44.0	5.9	25	65

4 APPLICATION

4.1 3-D topography/bathymetry, water layer and sediment effects—a case study of the 2016/10/27 M_w6.0 off coast southern Chile earthquake

One important potential application of our approach is the study of subduction zones, where megathrust earthquakes, some of the most powerful and destructive types of earthquakes on Earth, occur. The updip near-trench earthquakes are of particular importance for understanding rupture mechanics and the tsunami generation. However, the source parameters of offshore earthquakes are usually not well constrained due to the lack of seismic stations and geodetic measurements near the trenches, as well as inadequate incorporation of the complex near-trench structures in synthetic waveform calculation.

As an example, we study a shallow thrust earthquake near the southern Peru–Chile trench (Table 1) to show the effects of 3-D source-side structures, including ocean water, sediment and bathymetry with a strong gradient. The GCMT (Global Centroid Moment Tensor, Ekström *et al.* 2012) centroid location (S33.83°, W72.75°) of the earthquake is about 38 km away from the trench axis (Fig. 10a). With a M_w of 6.0, the earthquake produced high signal-to-noise ratio teleseismic *P*-waves. Strong *P*-wave codas are observed for this earthquake, even at relatively long periods (10–100 s) (Fig. 11a). At azimuths around 360° and 180°, the amplitudes of the coda waves are comparable with, or even larger than, the direct *P*-waves. They persist for longer than 90 s after the direct *P*-waves. High coherency of the coda waves across stations at different distances and azimuths indicates an origin of source-side effects rather than 3-D heterogeneities in the deep Earth or near the receivers. These features cannot be explained by a 1-D model, because its corresponding *P*-wave trains are overly simplistic.

Compared with heterogeneous crust, ocean water is much more homogeneous and has negligible attenuation. Therefore, seismic waves in ocean water can reverberate multiple times and be observed on teleseismic stations (Chu *et al.* 2011). To compute the hybrid synthetics, we take the earthquake centroid location as a centre of the SEM box and cut out a 5° (Longitude) × 5° (Latitude) × 120 km (depth) volume

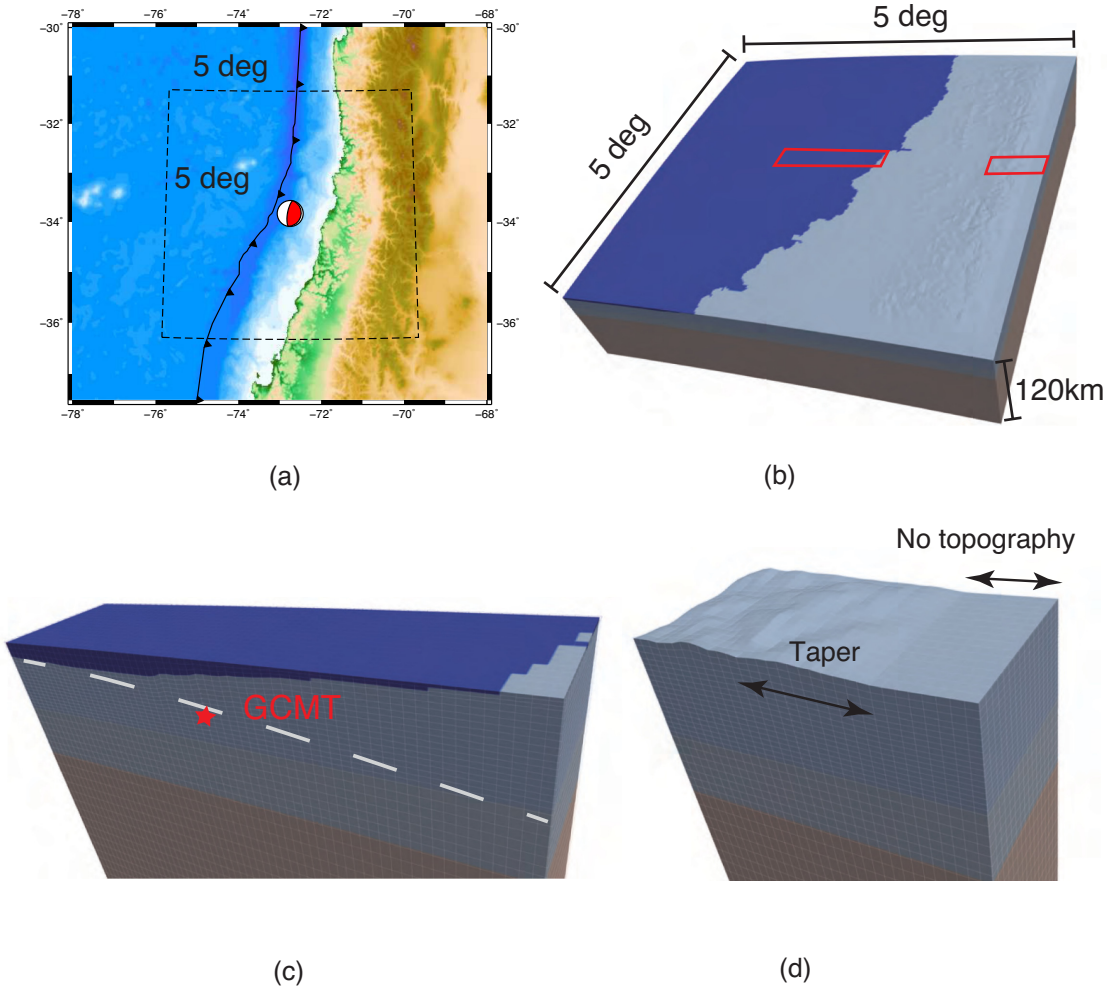

Figure 10. Map and SEM model. (a) Map of the southern Chile. We outline the trench trace based on the bathymetry features. The beach ball shows the GCMT solution. (b) The SEM box (black dashed line in Fig. 10a). (c) Part of meshing near the trench (the left red box in Fig. 10b). The grey dashed line shows an estimated depth of the top slab interface and the GCMT centroid location is about 2 km below the estimated slab interface. (d) Topography taper near the boundary of SEM box (the right red box in Fig. 10b). The topography is tapered to zero over a 12 elements wide transition zone.

from the globe for SEM calculation. We mesh the source region with 30 arc-second resolution topography/bathymetry (Figs 10a and b). The deep bathymetry (e.g. >1500 m) is exactly honoured and the shallow and smoothly varying bathymetry (e.g. <1500 m) near the coast is approximated by stepped grids (Fig. 10c). In order to match the 1-D background model, topography is tapered to zero at the boundaries of the SEM box (Fig. 10d). Another reason for adding this taper is to produce topography-free meshes on the coupling interfaces. Thus, all the vertical *i*th coupling meshes have the same depth and contribute only one member to the depth table, which makes the table length as short as possible and simplifies the DSM computation. According to the coupling theory, properties of the SEM box are required to match the 1-D DSM model on the interfacing boundary. However, part of the present model is composed of a water layer that extends to the sides of the SEM (Fig. 10b), which does not match the 1-D model. Nevertheless, we use this model here and ignore any contributions from the acoustic coupling faces into eq. (9). A detailed discussion regarding this issue is presented in the following sediment case.

Fig. 11 shows the data, 3-D hybrid synthetics and DSM 1-D synthetics, in the frequency range of 0.01–0.1 Hz. Compared with 1-D synthetics, the effects of water and topography/bathymetry do distort the direct *P*-waves and generate some coda waves. The distortion and coda waves are strongest near azimuth ∼360°, that is consistent with the data. However, the coda waves in the 3-D synthetics are not as strong as the data.

Apart from water and topography/bathymetry effects, sediment plays another important role in coda wave generation (Okamoto 1993). The sediment distribution and thickness in Peru-Chile subduction system change dramatically across the Juan Fernandez ridge (Schweller *et al.* 1981). For example, the northern Chile subduction zone has very thin offshore sediments, in contrast with much thicker offshore sediments in the southern Chile zone. A sediment layer up to a thickness of 2.3 km covers a width of more than 25 km across the trench (von Huene *et al.* 1997; Laursen *et al.* 2002) near the epicentre of the earthquake. We incorporate this sediment layer into SEM model using a width of 25 km and a thickness which linearly increases from 0 km at the trench axis to a maximum value of 2.3 km towards the coast. We also place a constant 1 km thick sediment layer on the shelf (Figs 12a and c). We take models by Hamilton (1976, 1979) to form Vp, Vs and

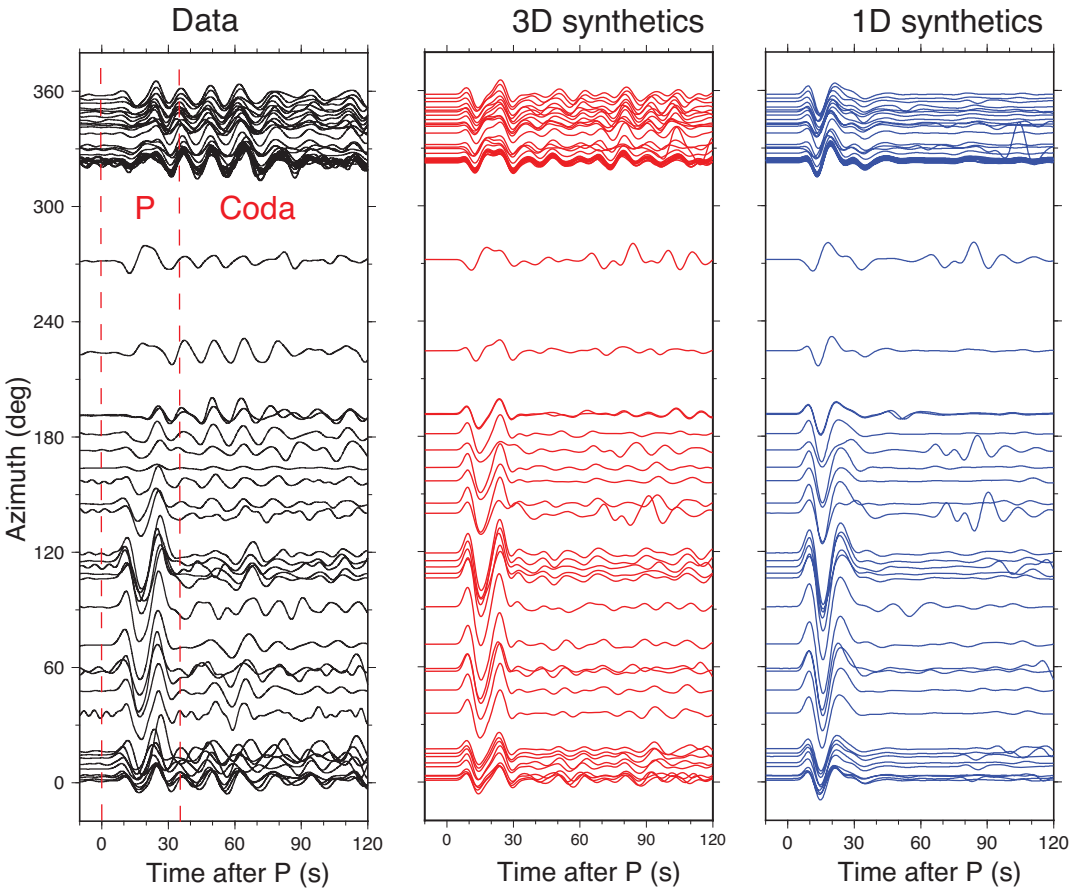

Figure 11. Data, 3-D synthetics and 1-D synthetics (0.01–0.1 Hz). (a) Displacement seismogram data. (b) Hybrid synthetics including the 3-D effects of water and topography/bathymetry. (c) 1-D synthetics.

density in the top 1 km sediment and extend the profiles to greater depths using the gradients at 1 km (Fig. 12b). Considering the numerical requirement of SEM simulation, Vs is limited to 500 m s^{-1}.

Fig. 12(d) shows the corresponding synthetics, in which the direct *P*-waves are similar to those in Fig. 11(b). However, the sediment layer does lead to longer coda durations and larger coda amplitudes, which significantly improves the fit to the data. The improvements can be seen at almost every azimuth, though we still fail to fit the data wiggle by wiggle. This is not unexpected, considering the uncertainty of GCMT source parameters (both focal mechanism and location) and oversimplified source-side model (e.g. we ignore along trench variation of sediment thickness). For example, both 1-D (Fig. 11c) and 3-D synthetics (Figs 11 b and 12d) near the azimuth of 180° show larger direct *P*-wave amplitudes than the data. These over-predictions might be due to errors in the GCMT solution, most likely the dip angle. For this case, if we assume the earthquake occurring on the slab interface, the 17° dip angle of the GCMT solution is steeper than the estimated value of about 11° in von Huene *et al.* (1997) and Laursen *et al.* (2002) (Fig. 12c, estimated from the seismic reflection profiles). On the other hand, the depth of the GCMT solution is 12 km, which is the minimum allowed depth in the GCMT inversion (Ekström *et al.* 2012). Thus the true centroid depth may be shallower (Fig. 12c) or the horizontal location may be closer to the coast, either of which could place the centroid location on the slab interface. Moreover, other 3-D complexities, such as the subducting slab and the accretionary prism, are not incorporated here. The presence of an accretionary prism, which has low seismic velocity and density, has been confirmed in this region by the CONDOR experiment (von Huene *et al.* 1997). The slab, composed of oceanic crust and lithosphere, also has a velocity structure different from our simplified model. Both of these factors would introduce additional waveform complexities in the synthetics.

In the above two sets of models, the ocean is abruptly truncated at the sides of SEM box. We argue that the consequent numerical errors are small for teleseismic *P*-waves, because the ray paths of teleseismic *P*-waves are nearly vertical at the source-side. Also, these ocean truncations are more than 2.5° away from the epicentre, so the scattered seismic waves caused by the truncation are expected to be small or arrive much later than the direct *P*-waves. They might be more important for the analysis of surface waves with horizontal ray paths, compared with teleseismic body waves. In order to further study this issue, we add solid media walls on the sides of the ocean and run the simulation again (see supplementary material). Comparing the two sets of synthetics shows only small differences, that further validates the synthetics in Fig. 12(d), at least in the time window 60 s after the direct *P*-waves.

In summary, 3-D effects of bathymetry/topography, a sediment layer, and ocean water can distort direct *P*-waves and produce strong coda waves for shallow offshore earthquakes that are close to trench, even at relatively long period bands (e.g. 0.01–0.1 Hz). These 3-D

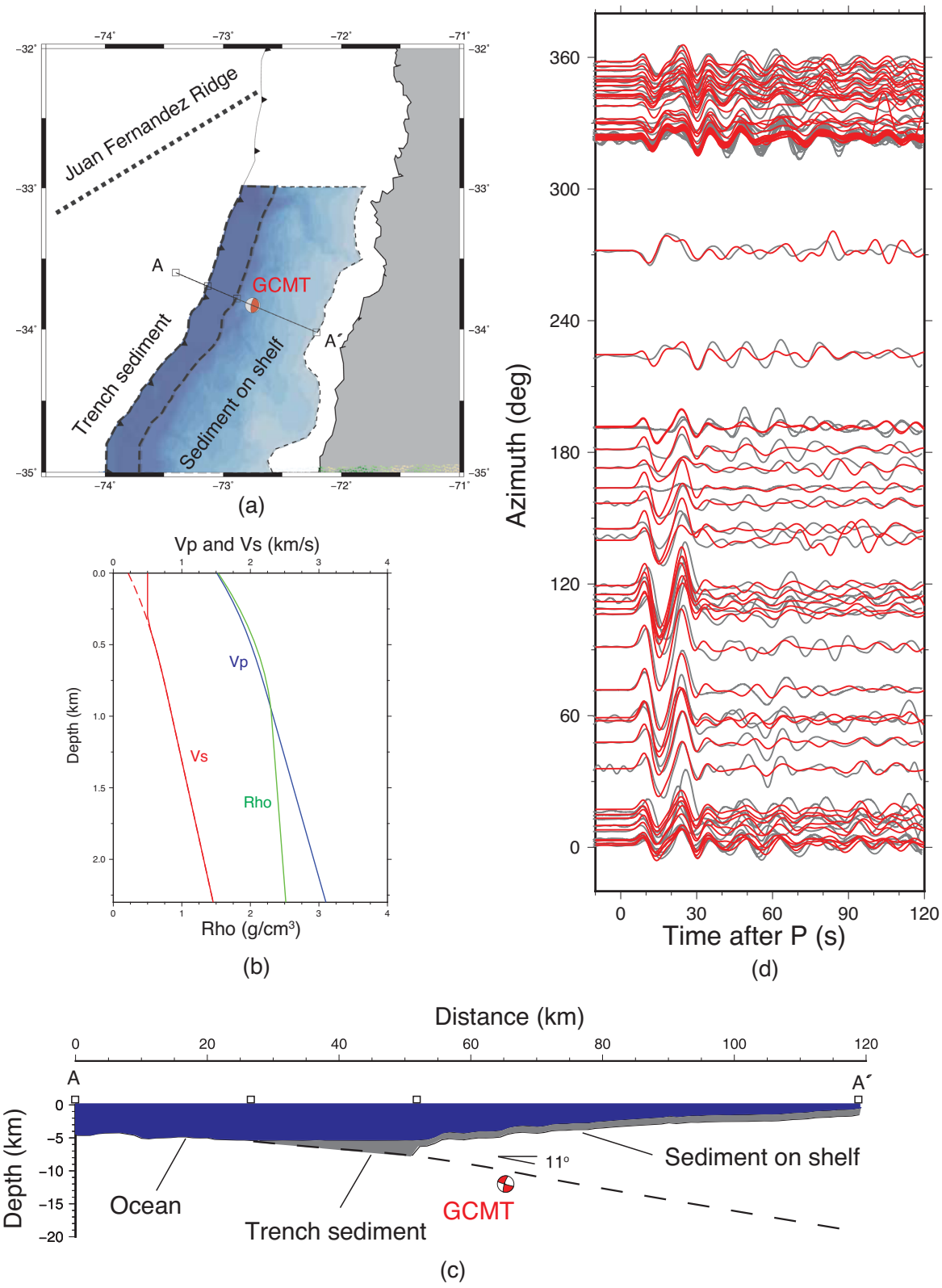

Figure 12. Sediment effects. (a) Map of the southern Chile. The trench sediment band starts at the trench axis and extends 25 km toward the coast. The right boundary of the sediment band on the shelf is simply defined as the 500 m bathymetry contour. A detailed depth profile of the sediment configurations is shown in (c). (b) Depth profiles of sediment seismic structure. The Vs below 500 m s^{-1} (red dashed line) in the most top sediment is replaced by 500 m s^{-1} (red line). (c) A depth profile subperpendicular to the trench axis (A-A´ in a). The blue layer represents ocean water and the grey shows sediment layer. The trench sediment starts at the trench and linearly increases to its maximum thickness 2.3 km. The sediment on the shelf has a constant thickness of 1 km, although the reflection/refraction profiles show varying thickness. (d) Data (grey) and synthetics (red) (0.01–0.1 Hz).

effects may bias the results of source parameter inversions at these period ranges, such as GCMT inversion, which does not take into account these effects during the synthetic calculation. Thus, the impact of the 3-D source-side structures on source parameter analysis must be further investigated. Here we show an example of a megathrust earthquake in the southern Chile, where thick sediment exists. In another paper (Qian *et al.* in preparation), we carefully investigate two earthquakes offshore northern Chile, where the sediment layer is very thin thus negligible at relatively long periods (e.g. > 10 s). There we obtain much better fit to the data. Globally, the type and thickness of sediments at trenches vary from one subduction zone to the other (see compilations of Clift & Vannucchi 2004; Heuret *et al.* 2012; Laske *et al.* 2013; Plank 2014). For example, terrigenous sediments with a thickness larger than 3 km are deposited at trenches of Andaman and Makran, where the plate convergent rates are high. The trenches of southern Antilles, central and southern Chile, eastern Alaska and Sumatra are also filled with a thick layer of sediment (>1 km). For the above regions, thick sediments can produce significant 3D effects on teleseismic waves. In contrast, sediments are relatively thin (<1 km) at trenches of Honshu, Kuril, Mexico, Costa-Rica, Peru and northern Chile. Note that, the estimated thickness for the same trench might be different from one compilation to the other, because different seismic-reflection lines are chosen.

4.2 Simulation of multipathing effects of slab—a case study of the 2009/09/10 M_w5.9 Sea of Okhotsk earthquake

Due to the critical roles of slabs in our dynamic Earth system, tremendous efforts have been made to sharpen seismic imaging of slab structures. Limited by the smoothing constraints, conventional travel time tomography techniques usually smear sharp or detailed structures, and may underestimate the maximum velocity anomaly. As a new type of observation, Zhan *et al.* (2014) discovered multipathing phenomenon of teleseismic *P*-waves traveling within and out of a slab, and demonstrated its potential in imaging a sharp slab structure. A seismically fast core (∼5 per cent positive Vp anomaly) of the slab beneath the Sea of Okhotsk was proposed to explain the multipathing teleseismic waves around the slab downdip azimuth. However, the 2-D FD method adopted in that paper only allows us to investigate the data around the downdip azimuth, and it is unable to simulate the waves off the downdip azimuth. Here we show the capability of our hybrid method to model the data off the downdip azimuth.

We first create an 8° (trench parallel) × 10° (downdip) × 800 km (depth) SEM box located in the region of the Sea of Okhotsk (Figs 13a and b). The SEM box is then rotated by 41° counterclockwise to make its horizontal edges roughly follow the trench parallel and downdip directions respectively. Next a model of a 120 km thick slab is incorporated into the SEM box. The depth of the top slab interface is based on the Slab1.0 model (Hayes *et al.* 2012). According to the results by Zhan *et al.* (2014), we introduce a triangular-shaped high velocity anomaly profile across the slab with a maximum perturbation of 5 per cent in the slab centre, which linearly decays to the background velocity toward the top and bottom interface (Fig. 13c). In order to match the background 1-D model, the structural anomaly of the slab is tapered toward the boundaries of the SEM box. The bottom edge of the deep subducted slab is also tapered to avoid strong scattering or reflection waves.

We focus on the 2009/09/10 shallow megathrust earthquake, from which Zhan *et al.* (2014) observed obvious broadened teleseismic *P*-waves. We use the GCMT solution as source parameters of the event (Table 1), but replace its duration of 4.6 s with 2.0 s, which is more likely, based on the observed waveform data. Indeed, GCMT provides a duration value by simply scaling the scalar moment, which can significantly deviate from the true value. The SEM box is meshed with 176 (trench parallel) × 192 (downdip) × 104 (depth) elements (Fig. 13), allowing the resolution of seismic waves with a maximum frequency up to 0.5 Hz. Here we use 256 processor cores to obtain the local 3D wavefield with a time length of 500 s, which is sufficiently long to investigate the direct *P*-waves and its depth phases. It took the 256 processors about 6 hr to simulate the seismic wavefield with 12500 time steps. Generating these teleseismic synthetics through SEM simulation in the entire Earth, or even just one portion of the Earth (e.g. 90° × 90° × 2891 km), would increase the computation time by at least two orders of magnitude.

Fig. 14 shows record section for stations (Supporting Information Fig. S10) within 45° of the downdip azimuth (315°), which has been analysed via 2-D FD modelling by Zhan *et al.* (2014). In the data, we can see the broadened direct *P*-waves and associated depth phases at distances less than 70° (Fig. 14a), and relatively impulsive signals at distances greater than 70°. Similar to previous results (Zhan *et al.* 2014), our hybrid 3D synthetics reproduce the multipathing effects caused by the slab. Accompanied with the broadening effects, we also see a distance dependent arrival time advancement of the direct *P*-waves, due to the high velocity anomaly of slab. Such distance dependent effects of broadening and arrival time advancement can be well explained by the ray paths in Fig. 13(c). In contrast, 1-D synthetics are simply composed of a few impulsive signals and show high waveform similarity across stations at different distances. We note that there are some waveform differences between the 3-D synthetics shown here and the 2-D results in Zhan *et al.* (2014), mainly due to the slab geometry correction made in (Zhan *et al.* 2014), different source parameters, and probable discrepancies between 2-D and 3-D simulations.

To investigate effects of the slab on waveforms off the downdip azimuth, we collect global teleseismic data within a distance range of 45°–60° (Supporting Information Fig. S11), and plotted an azimuth record section in Fig. 15(a). The data gap around the azimuth of 120° is due to the lack of good quality data in the Pacific ocean (Supporting Information Fig. S11). We first compare the data with 1-D synthetics. The 1-D waveforms at different azimuths show significant variations (Fig. 15c), which are mainly controlled by the radiation pattern of the focal mechanism. For example, the depth phase pP is large within the azimuth range of 30°–225° while sP has large amplitudes on other azimuths. This pattern is generally consistent with the data. However, 1-D synthetics cannot explain the broadened *P*-waves and depth phase sP around the downdip azimuth of 315°. The 3-D synthetics successfully duplicate the multipathing features (Fig. 15b). More specifically, the multipathing effects on the *P*-waves and s*P*-waves appear in the azimuth ranges of 255°–360° and 0°–15°. We observe an abrupt transition from broadened waveforms to normal waveforms at the azimuths of 15° and 255°. Theoretically, where and how these transitions occur

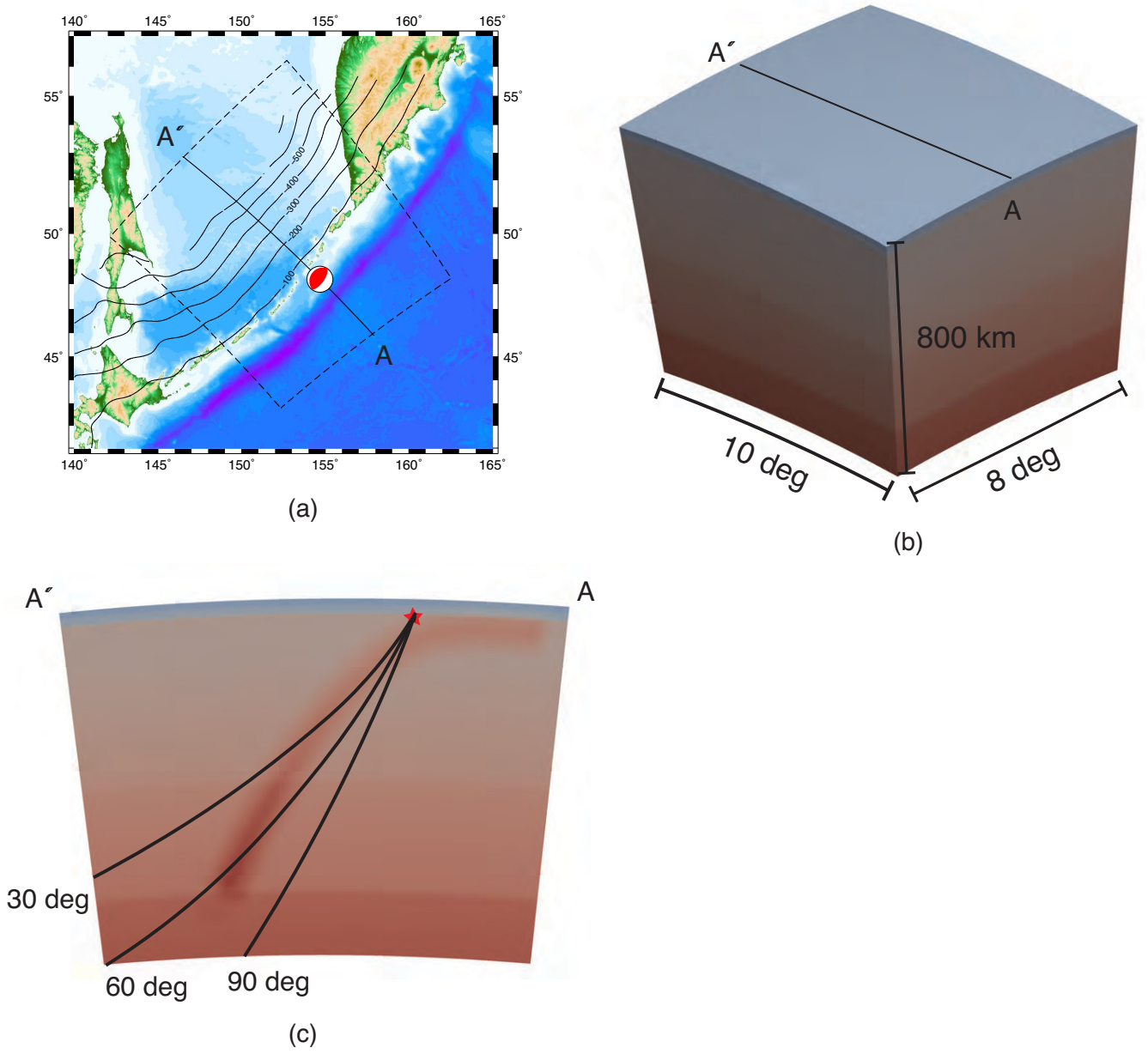

Figure 13. Model setup. (a) Map of the Sea of Okhotsk. The blacked lines represent the depth contours of slab (Hayes *et al.* 2012). The beach ball shows the GCMT solution. (b) The SEM box. (c) A depth profile of Vp along the slab downdip direction (A-A´ profile in a and b). The slab has a thickness of 120 km and high velocity anomaly. For visualization reason, the velocity anomaly of slab is exaggerated by a factor of four. The black lines show the three ray paths of the direct *P*-waves at distances 30°, 60° and 90°.

depends on the specific distance range and here we only show the results for a distance range of 45°–60°. As we mentioned above, the multipathing effects are concomitant with arrival time advancements, which could be up to 1.5 s at the azimuth of 315°.

Although the general pattern of multipathing effects in the 3-D synthetics and data are well matched in the distance and azimuth profiles, there are still large differences between the 3-D synthetics and data. Possible reasons for these errors include inaccurate geometry and structures of the slab, and/or an inaccurate GCMT solution. For example, the dip angle of the deep slab model seems too steep, which may result in insufficient broadening effects at the distance around 40° (Fig. 14). This was pointed out by Zhan *et al.* (2014) and a correction was made to the dip angle based on the spatial distribution of deep seismicity. The GCMT solution may be biased by shallow subduction structures. For example, even the polarities of the direct *P*-waves at azimuths of about 60° are opposite in the data and synthetics, indicating either a biased focal mechanism and/or an over-simplified slab model.

We demonstrated the effects of 3-D heterogeneities near the trench on teleseismic data in Section 4.1, and the example here shows more complexities could be caused by the slab itself. Any of these issues could bias the results of source parameter inversions based on 1-D synthetics. Thus, more detailed studies of the 3-D source-side structures are necessary for better understanding of slab structures and source parameter inversions.

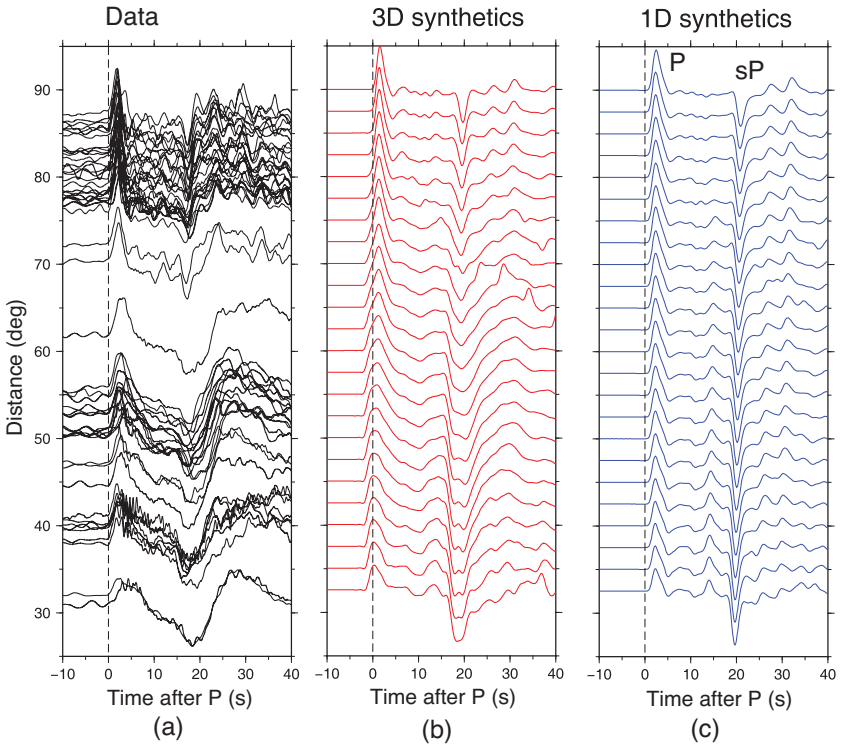

Figure 14. Distance profiles of displacement data, 3-D synthetics and 1-D synthetics. The time zero in the data is hand-picked *P*-wave onsets. The time zeros in the 3-D and 1-D synthetics are the direct *P*-wave arrivals predicted by IASP91.

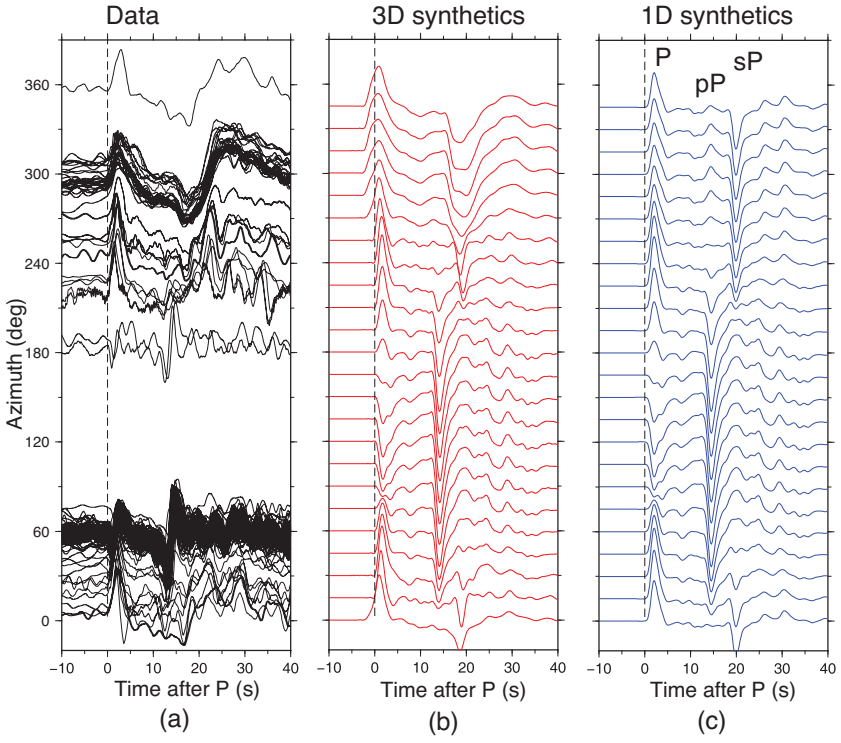

Figure 15. Azimuth profiles of data, 3-D synthetics and 1-D synthetics. The time zero in the data is hand-picked *P*-wave onsets. The time zeros in the 3-D and 1-D synthetics are the direct *P*-wave arrivals predicted by IASP91.

5 CONCLUSION

We developed an SEM-DSM hybrid method to efficiently compute teleseismic waves with 3-D source-side structures. The synthetics of our hybrid method were benchmarked against DSM synthetics using the IASP91 1-D model, as well as 3-D SEM models that include topography and a water layer. Our hybrid method combines the advantages of DSM and SEM. The 3-D SEM simulation at the source-side allows the incorporation of various structure complexities, including anisotropy, topography/bathymetry, ocean water, sediments and subudcting slabs. Compared to global SEM simulations, the computational time and memory requirement are reduced substantially by our method. Our hybrid method offers an efficient tool to compute teleseismograms with 3-D source-side structures, with the understanding that the truncation of the SEM calculation may produce some numerical noise. While other numerical approaches are better suited to handle low frequency global waveform simulations, our hybrid method is more efficient at simulating higher frequency teleseismic synthetics.

Our hybrid method can be applied to refining earthquake source parameters with 3-D source-side structures, in particular for subduction zone and mid-ocean ridge earthquakes. We presented two examples of earthquakes in subduction zones. In the first example of a shallow megathrust earthquake in southern Chile, we observe strong *P*-wave codas, even at a relatively long period band (10–100 s). These coda waves are coherent across different azimuths and distances, which are well explained by the 3-D topography/bathymetry, ocean water, and sediment layer near the trench. In the other example of a Sea of Okhotsk earthquake, we modelled the multipathing effects on teleseismic *P*-waves caused by the high velocity anomaly of the slab. In the latter case, the SEM box has a maximum depth of 800 km and our hybrid method saves more than two orders of magnitude computational time when compared to SEM simulation alone.

In summary, our hybrid method provides an efficient tool to reliably model 3-D source-side effects, in particular complex subduction zone structures, via the accurate simulation of various teleseismic phases (e.g. P, S, PcP, PKiKP, SKS and so on) where it has previously been too costly to do so. This tool would be helpful for investigating source parameters with 3-D source-side structures, imaging source-side structures, and solving other problems related to 3-D source-side structures. Our hybrid method has been successfully used to investigate the effects of topography (Wang *et al.* 2017) and ocean water and sediment (Wang *et al.* 2018) on teleseismic *P*-waves. However, our hybrid method only addresses source-side complexities and might not work for cases where both source and receiver regions are complicated. With ever increasing computation capability, fully global 3-D simulations will be feasible in the future for high frequency waves (a few Hz) at teleseismic distances.

ACKNOWLEDGEMENTS

We are grateful for reviews from Sébastien Chevrot and another anonymous reviewer which helped to improve the manuscript. We thank Joel D. Simon and Frederik J. Simons for suggestions to improve this manuscript. We are thankful to Nozomu Takeuchi for providing the DSM software (http://www.eri.u-tokyo.ac.jp/people/takeuchi/software/index.html). Our code will be posted on https://github.com/wenbowu-geo. This work was supported by funding from National Basic Research Program of China (973 Program) through grant 2014CB845901. SW is supported by the internal grant (M4430255) of Earth Observatory of Singapore. The authors acknowledge the use of the GMT (Wessel & Smith 1998) and SAC (Goldstein *et al.* 2003) software packages. The seismic waveform data used in this study were obtained from the Incorporated Research Institutions for Seismology (IRIS) Data Management Center(http://dx.doi.org/doi:10.7914/SN/II).

REFERENCES

Aki, K. & Richards, P.G., 2002. *Quantitative Seismology,* 2nd edn, University Science Books.

Alterman, Z. & Karal, F., 1968. Propagation of elastic waves in layered media by finite difference methods, *Bull. seism. Soc. Am.,* **58**(1), 367–398.

Baker, B. & Roecker, S., 2014. A full waveform tomography algorithm for teleseismic body and surface waves in 2.5 dimensions, *Geophys. J. Int.,* **198**(3), 1775–1794.

Beller, S., Monteiller, V., Operto, S., Nolet, G., Paul, A. & Zhao, L., 2018. Lithospheric architecture of the South-Western Alps revealed by multi-parameter teleseismic full-waveform inversion, *Geophys. J. Int.,* **212**(2), 1369–1388.

Bielak, J. & Christiano, P., 1984. On the effective seismic input for non-linear soil-structure interaction systems, *Earthq. Eng. Struct. Dyn.,* **12**(1), 107–119.

Bielak, J., Loukakis, K., Hisada, Y. & Yoshimura, C., 2003. Domain reduction method for three-dimensional earthquake modeling in localized regions, Part I: Theory, *Bull. seism. Soc. Am.,* **93**(2), 817–824.

Borisov, D., Singh, S.C. & Fuji, N., 2015. An efficient method of 3-D elastic full waveform inversion using a finite-difference injection method for time-lapse imaging, *Geophys. J. Int.,* **202**(3), 1908–1922.

Chu, R., Wei, S., Helmberger, D.V., Zhan, Z., Zhu, L. & Kanamori, H., 2011. Initiation of the great *M*w 9.0 Tohoku–Oki earthquake, *Earth planet. Sci. Lett.,* **308**(3-4), 277–283.

Clift, P. & Vannucchi, P., 2004. Controls on tectonic accretion versus erosion in subduction zones: implications for the origin and recycling of the continental crust, *Rev. Geophys.,* **42**(2),

Clouzet, P., Masson, Y. & Romanowicz, B., 2018. Box tomography: first application to the imaging of upper-mantle shear velocity and radial anisotropy structure beneath the North American continent, *Geophys. J. Int.,* **213**(3), 1849–1875.

Dahlen, F. & Tromp, J., 1998. *Theoretical Global Seismology,* Princeton University Press.

Ekström, G., Nettles, M. & Dziewoński, A., 2012. The global CMT project 2004–2010: centroid-moment tensors for 13 017 earthquakes, *Phys. Earth planet. Inter.,* **200-201,** 1–9.

Fäh, D., Suhadolc, P., Mueller, S. & Panza, G.F., 1994. A hybrid method for the estimation of ground motion in sedimentary basins: quantitative modeling for Mexico City, *Bull. seism. Soc. Am.,* **84**(2), 383–399.

Fan, W. & Shearer, P.M., 2016. Local near instantaneously dynamically triggered aftershocks of large earthquakes, *Science,* **353**(6304), 1133–1136.

Fuji, N., Chevrot, S., Zhao, L., Geller, R.J. & Kawai, K., 2012. Finite-frequency structural sensitivities of short-period compressional body waves, *Geophys. J. Int.,* **190**(1), 522–540.

Geller, R.J. & Ohminato, T., 1994. Computation of synthetic seismograms and their partial derivatives for heterogeneous media with arbitrary natural boundary conditions using the Direct Solution Method, *Geophys. J. Int.,* **116**(2), 421–446.

Geller, R.J. & Takeuchi, N., 1995. A new method for computing highly accurate DSM synthetic seismograms, *Geophys. J. Int.,* **123**(2), 449–470.
Goldstein, P., Dodge, D., Firpo, M. & Minner, L., 2003. SAC2000: signal processing and analysis tools for seismologists and engineers, in *The IASPEI International Handbook of Earthquake and Engineering Seismology,* Vol. **81,** pp. 1613–1620, eds Lee, W.H.K., Kanamori, H., Jennings, P.C. & Kisslinger, C., Academic Press.
Hamilton, E.L., 1976. Variations of density and porosity with depth in deep-sea sediments, *J. Sediment. Res.,* **46**(2), 280–300.
Hamilton, E.L., 1979. Vp/Vs and Poisson's ratios in marine sediments and rocks, *J. accoust. Soc. Am.,* **66**(4), 1093–1101.
Hayes, G.P., Wald, D.J. & Johnson, R.L., 2012. Slab1.0: A three-dimensional model of global subduction zone geometries, *J. geophys. Res.,* **117**(B1), B01302.
Heuret, A., Conrad, C.P., Funiciello, F., Lallemand, S. & Sandri, L., 2012. Relation between subduction megathrust earthquakes, trench sediment thickness and upper plate strain, *Geophys. Res. Lett.,* **39**(5), L05304.
Igel, H., Nissen-Meyer, T. & Jahnke, G., 2002. Wave propagation in 3D spherical sections: effects of subduction zones, *Phys. Earth planet. Inter.,* **132**(1-3), 219–234.
Kawai, K., Takeuchi, N. & Geller, R.J., 2006. Complete synthetic seismograms up to 2 Hz for transversely isotropic spherically symmetric media, *Geophys. J. Int.,* **164**(2), 411–424.
Kennett, B. L.N. & Engdahl, E.R., 1991. Traveltimes for global earthquake location and phase identification, *Geophys. J. Int.,* **105**(2), 429–465.
Komatitsch, D., 2004. Simulations of ground motion in the Los Angeles Basin based upon the spectral-element method, *Bull. seism. Soc. Am.,* **94**(1), 187–206.
Komatitsch, D. & Tromp, J., 1999. Introduction to the spectral element method for three-dimensional seismic wave propagation, *Geophys. J. Int.,* **139**(3), 806–822.
Komatitsch, D. & Tromp, J., 2002. Spectral-element simulations of global seismic wave propagation-II. three-dimensional models, oceans, rotation and self-gravitation, *Geophys. J. Int.,* **150**(1), 303–318.
Komatitsch, D., Michéa, D. & Erlebacher, G., 2009. Porting a high-order finite-element earthquake modeling application to NVIDIA graphics cards using CUDA, *J. Parallel Distrib. Comput.,* **69**(5), 451–460.
Laske, G., Masters, G., Ma, Z. & Pasyanos, M., 2013. Update on CRUST1.0—A 1-degree global model of Earths crust, *Geophys. Res. Abstr.,* **15,** 2658.
Laursen, J., Scholl, D.W. & von Huene, R., 2002. Neotectonic deformation of the central Chile margin: deepwater forearc basin formation in response to hot spot ridge and seamount subduction, *Tectonics,* **21**(5), 1038.
Lay, T., Li, L. & Cheung, K.F., 2016. Modeling tsunami observations to evaluate a proposed late tsunami earthquake stage for the 16 September 2015 Illapel, Chile, M_w8.3 earthquake, *Geophys. Res. Lett.,* **43**(15), 7902–7912.
Lee, S.-J., Chan, Y.-C., Komatitsch, D., Huang, B.-S. & Tromp, J., 2009. Effects of realistic surface topography on seismic ground motion in the Yangminshan region of Taiwan based upon the spectral-element method and LiDAR DTM, *Bull. seism. Soc. Am.,* **99**(2A), 681–693.
Lee, S.-J., Yeh, T.-Y., Lin, T.-C., Lin, Y.-Y., Song, T.-R.A. & Huang, B.-S., 2016. Two-stage composite megathrust rupture of the 2015 M_w8.4 Illapel, Chile, earthquake identified by spectral-element inversion of teleseismic waves, *Geophys. Res. Lett.,* **43**(10), 4979–4985.
Masson, Y. & Romanowicz, B., 2017a. Box tomography: localized imaging of remote targets buried in an unknown medium, a step forward for understanding key structures in the deep Earth, *Geophys. J. Int.,* **211**(1), 141–163.
Masson, Y. & Romanowicz, B., 2017b. Fast computation of synthetic seismograms within a medium containing remote localized perturbations: a numerical solution to the scattering problem, *Geophys. J. Int.,* **208**(2), 674–692.
Masson, Y., Cupillard, P., Capdeville, Y. & Romanowicz, B., 2014. On the numerical implementation of time-reversal mirrors for tomographic imaging, *Geophys. J. Int.,* **196**(3), 1580–1599.
Melgar, D. *et al.*, 2016. Slip segmentation and slow rupture to the trench during the 2015, *M*w8.3 Illapel, Chile earthquake, *Geophys. Res. Lett.,* **43**(3), 961–966.
Meng, L., Ampuero, J.-P., Luo, Y., Wu, W. & Ni, S., 2012. Mitigating artifacts in back-projection source imaging with implications for frequency-dependent properties of the Tohoku-Oki earthquake, *Earth Planets Space,* **64**(12), 1101–1109.
Monteiller, V., Chevrot, S., Komatitsch, D. & Fuji, N., 2013. A hybrid method to compute short-period synthetic seismograms of teleseismic body waves in a 3-D regional model, *Geophys. J. Int.,* **192**(1), 230–247.
Monteiller, V., Chevrot, S., Komatitsch, D. & Wang, Y., 2015. Three-dimensional full waveform inversion of short-period teleseismic wavefields based upon the SEM–DSM hybrid method, *Geophys. J. Int.,* **202**(2), 811–827.
Okamoto, T., 1993. Effects of sedimentary structure and bathymetry near the source on teleseismic *P* waveforms from shallow subduction zone earthquakes, *Geophys. J. Int.,* **112**(3), 471–480.
Okamoto, T., 1994. Teleseismic synthetics obtained from 3-D calculations in 2-D media, *Geophys. J. Int.,* **118**(3), 613–622.
Okamoto, T. & Takenaka, H., 2009. Waveform inversion for slip distribution of the 2006 Java tsunami earthquake by using 2.5D finite-difference Green's function, *Earth Planets Space,* **61**(5), e17–e20.
Opršal, I., Matyska, C. & Irikura, K., 2009. The source-box wave propagation hybrid methods: general formulation and implementation, *Geophys. J. Int.,* **176**(2), 555–564.
Plank, T., 2014. The Chemical Composition of Subducting Sediments, in *Treatise on Geochemistry,* pp. 607–629, eds Holland, H. & Turekian, K., Elsevier.
Robertsson, J.O.A. & Chapman, C.H., 2000. An efficient method for calculating finite-difference seismograms after model alterations, *Geophysics,* **65**(3), 907–918.
Schweller, W.J., Kulm, L.D. & Prince, R.A., 1981. Tectonics, structure, and sedimentary framework of the Peru-Chile Trench, in *Nazca Plate: Crustal Formation and Andean Convergence,* pp. 323–350, eds Kulm, L.D., Prince, R.A., Kulm, L.V.D., Dymond, J., Dasch, E.J., Hussong, D.M. & Roderick, R., Geological Society of America.
Silver, P.G. & Chan, W.W., 1986. Observations of body wave multipathing from broadband seismograms: evidence for lower mantle slab penetration beneath the Sea of Okhotsk, *J. geophys. Res.,* **91**(B14), 13787 .
Stewart, G.S. & Helmberger, D.V., 1981. The Bermuda earthquake of March 24, 1978: a significant oceanic intraplate event, *J. geophys. Res.,* **86**(B8), 7027, .
Takeuchi, N., Geller, R.J. & Cummins, P.R., 1996. Highly accurate *P–SV* complete synthetic seismograms using modified DSM operators, *Geophys. Res. Lett.,* **23**(10), 1175–1178.
Tape, C., Liu, Q., Maggi, A. & Tromp, J., 2009. Adjoint Tomography of the Southern California Crust, *Science,* **325**(5943), 988–992.
Tong, P., Chen, C.-w., Komatitsch, D., Basini, P. & Liu, Q., 2014a. High-resolution seismic array imaging based on an SEM-FK hybrid method, *Geophys. J. Int.,* **197**(1), 369–395.
Tong, P., Komatitsch, D., Tseng, T.-L., Hung, S.-H., Chen, C.-W., Basini, P. & Liu, Q., 2014b. A 3-D spectral-element and frequency-wave number hybrid method for high-resolution seismic array imaging, *Geophys. Res. Lett.,* **41**(20), 7025–7034.
Tromp, J., Komatitsch, D. & Liu, Q., 2008. Spectral-element and adjoint methods in seismology, *Commun. Comput. Phys.,* **3**(1), 1–32.
van Manen, D.-J., Robertsson, J. O.A. & Curtis, A., 2007. Exact wave field simulation for finite-volume scattering problems, *J. accoust. Soc. Am.,* **122**(4), EL115–EL121.
Vidale, J.E., Williams, Q. & Houston, H., 1991. Waveform effects of a metastable olivine tongue in subducting slabs, *Geophys. Res. Lett.,* **18**(12), 2201–2204.
von Huene, R., Corvalán, J., Flueh, E.R., Hinz, K., Korstgard, J., Ranero, C.R. & Weinrebe, W., 1997. Tectonic control of the subducting Juan Fernández Ridge on the Andean margin near Valparaiso, Chile, *Tectonics,* **16**(3), 474–488.

Wang, X., Wei, S. & Wu, W., 2017. Double-ramp on the Main Himalayan Thrust revealed by broadband waveform modeling of the 2015 Gorkha earthquake sequence, *Earth planet. Sci. Lett.,* **473,** 83–93.

Wang, X., Bradley, K.E., Wei, S. & Wu, W., 2018. Active backstop faults in the Mentawai region of Sumatra, Indonesia, revealed by teleseismic broadband waveform modeling, *Earth planet. Sci. Lett.,* **483,** 29–38.

Wang, Y. *et al.*, 2016. The deep roots of the western Pyrenees revealed by full waveform inversion of teleseismic*P* waves, *Geology,* **44**(6), 475–478.

Wen, L. & Helmberger, D.V., 1998. A two-dimensional P-SV hybrid method and its application to modeling localized structures near the core-mantle boundary, *J. geophys. Res.,* **103**(B8), 17901–17918.

Wessel, P. & Smith, W.H., 1998. New, improved version of Generic Mapping Tools released, *EOS, Trans. Am. geophys. Un.,* **79**(47), 579–579.

Xie, Z., Komatitsch, D., Martin, R. & Matzen, R., 2014. Improved forward wave propagation and adjoint-based sensitivity kernel calculations using a numerically stable finite-element PML, *Geophys. J. Int.,* **198**(3), 1714–1747.

Yoshimura, C., Bielak, J., Hisada, Y. & Fernández, A., 2003. Domain reduction method for three-dimensional earthquake modeling in localized regions, part II: Verification and applications, *Bull. seism. Soc. Am.,* **93**(2), 825–841.

Zahradník, J. & Moczo, P., 1996. Hybrid seismic modeling based on discrete-wave number and finite-difference methods, *Pure appl. Geophys.,* **148**(1), 21–38.

Zhan, Z. *et al.*, 2012. Anomalously steep dips of earthquakes in the 2011 Tohoku-Oki source region and possible explanations, *Earth planet. Sci. Lett.,* **353-354,** 121–133.

Zhan, Z., Helmberger, D.V. & Li, D., 2014. Imaging subducted slab structure beneath the Sea of Okhotsk with teleseismic waveforms, *Phys. Earth planet. Inter.,* **232,** 30–35.

SUPPORTING INFORMATION

Supplementary data are available at *GJI* online.

Figure S1. Cumulative sums on the right rand side of eq. (12), for a distance of 3° (red line in the left figure) and 30° (red line in the right figure). For simplicity, we assume $4\pi c^2 = 1$. Thus, the theoretical value of $g(r, k)$ equals $\frac{1}{|\mathbf{r}-\mathbf{r_s}|} = \frac{1}{r\cos(\theta)}$ (red dashed lines), where $r = r_s = 6371\ km$ and θ is the distance. The oscillations of solutions are modulated by a amplitude decay factor $\frac{1}{\sqrt{l}}$ (black dashed lines) and the period of the oscillation is inversely proportional to their distances.

Figure S2. Oscillation behavior of DSM synthetic u_r (period T = 100 s) at large angular orders. An explosion source at a depth of 10 km is modeled and two teleseismic receivers are located at the same horizontal distance of 30°, but different depths (10 km in the left figure and 15 km in the right figure). The blue lines are imaginary parts and the red lines show real parts. The black dashed lines indicate $\frac{1}{\sqrt{2l+1}}(\frac{r}{r_s})^l$ decay shapes. The cumulative sums of real parts oscillate with a period of $\triangle l = 12$ (zoom-in insets), once they pass the threshold angular order $l_t = 97$.

Figure S3. Amplitude of the expansion coefficient c^{lmk1} (period T = 100 s), as a function of radius. An explosion source is placed at a radius of 6361 km, the same as Fig. S2. The dashed lines indicate the power function decay trends, which fit the data well on both sides of the source radius. The amplitude changes are disturbed around the discontinuities of seismic properties, such as the free surface and middle crust interface at a depth of 20 km.

Figure S4. Same as Fig. S2, but the source is a vertical single force at a depth of 0 km and the stations have depths of 1 km (left figure) and 10 km (right figure).

Figure S5. Same as Fig. S4, but the source is a vertical single force at a depth of 0 km.

Figure S6. Complex values of vertical displacement Green's functions at a depth of 80 km. The source is a vertical single force applied on the free surface. The left figure corresponds to the frequency of 0.1 Hz and the right figure shows the 1 Hz results. The solid lines are real parts and the dashed lines show imaginary parts.

Figure S7. Testing performances of Lagrange polynomial interpolations with different degrees. The black lines are the same as Fig. S6b. "nfit" represents the degree of Lagrange polynomial. The red points with a space of 0.015^o show the values used in interpolations.

Figure S8. Teleseismic stations (blue triangles) used in Fig. 11a. The red star shows the location of earthquake.

Figure S9. Testing the consequences of the mismatch between local SEM model and 1D DSM model on the coupling interface. (a) SEM model used in Fig. 12 of the main text. (b) Adding artificial solid media walls on the ocean sides of SEM box. (c) The red lines are synthetics for the model with ocean sides (Fig. S9a) and the blue lines show synthetics associated with the solid media wall model (Fig. S9b). They are pretty similar to each other and only small differences are visible in the time window 60 - 120 s.

Figure S10. Stations (blue triangles) used in Fig. 14. The red star shows the location of earthquake.

Figure S11. Stations (blue triangles) used in Fig. 15. The red star shows the location of earthquake.

Please note: Oxford University Press is not responsible for the content or functionality of any supporting materials supplied by the authors. Any queries (other than missing material) should be directed to the corresponding author for the article.

APPENDIX A: SINGLE FORCE EXCITATION

In coupling eq. (9), we need to compute the Green's functions excited by the three independent single forces. A detailed derivation of excitation terms due to a point source of moment tensor in DSM has been presented in previous literature (e.g. Kawai *et al.* 2006). Here we follow their work and derive source terms due to a single force excitation. Source terms corresponding to a single force excitation in DSM

can be written as

$$g^{lmk1} = \int_V (\mathbf{\Phi}^{klm1})^* \cdot \mathbf{f} \mathrm{d}V$$
$$= \int_V Y^{lm*}(\theta,\phi) X^k(r) f_r \delta(\mathbf{r}-\mathbf{r}_s) \mathrm{d}V \tag{A1}$$
$$= \delta_{kk_s} f_r Y^{lm*}(\theta,\phi)\Big|_{\theta=\theta_s,\phi=\phi_s}$$

$$g^{lmk2} = \int_V (\mathbf{\Phi}^{klm2})^* \cdot \mathbf{f} \mathrm{d}V$$
$$= \frac{\delta_{kk_s}}{\sqrt{l(l+1)}}\left[f_\theta \frac{\partial Y^{lm*}(\theta,\phi)}{\partial\theta}\Big|_{\theta=\theta_s,\phi=\phi_s} + f_\phi \frac{1}{\sin(\theta)} \frac{\partial Y^{lm*}(\theta,\phi)}{\partial\phi}\Big|_{\theta=\theta_s,\phi=\phi_s}\right] \tag{A2}$$

$$g^{lmk3} = \int_V (\mathbf{\Phi}^{klm3})^* \cdot \mathbf{f} \mathrm{d}V$$
$$= \frac{\delta_{kk_s}}{\sqrt{l(l+1)}}\left[f_\theta \frac{1}{\sin(\theta)} \frac{\partial Y^{lm*}(\theta,\phi)}{\partial\phi}\Big|_{\theta=\theta_s,\phi=\phi_s} - f_\phi \frac{\partial Y^{lm*}(\theta,\phi)}{\partial\theta}\Big|_{\theta=\theta_s,\phi=\phi_s}\right] \tag{A3}$$

Where $\mathbf{\Phi}^{klm1} = X^k(r)\mathbf{S}^{lm1}(\theta,\phi)$, $\mathbf{\Phi}^{klm2} = X^k(r)\mathbf{S}^{lm2}(\theta,\phi)$ and $\mathbf{\Phi}^{klm3} = X^k(r)\mathbf{T}^{lm}(\theta,\phi)$ are the three types of trial functions (see more details in Kawai *et al.* 2006). δ_{kk_s} means the source acting exactly on the radial kth node. In our scenario, it is the most top node on the free surface, where seismometers are usually located. Given a 1-D Earth model, specifying the single force at the pole ($\theta_s \to 0$) would significantly save the computational time, because eqs (A1)–(A3) are then non-zero only for $|m| \leq 1$. More specifically,

$$Y^{lm*}(\theta,\phi) = Z^{lm} e^{-im\phi} \tag{A4}$$

and

$$Z^{lm}(\theta) = (-1)^m \sqrt{\frac{(2l+1)(l-m)!}{4\pi(l+m)!}} P^{lm}(\cos(\theta)) \tag{A5}$$

where $P^{lm}(\cos(\theta))$ is the associated Legendre functions with an angular order l and an azimuthal order m. When $\theta = \theta_s \approx 0$ (see eq. B.62 on page 849 of Dahlen & Tromp 1998)

$$Z^{lm}(\theta) \approx \begin{cases} (-1)^m b^{lm} \theta^{|m|}; & if \ -l \leq m < 0 \\ b^{l0}[1 - \frac{1}{4} l(l+1)\theta^2]; & if \ m = 0 \\ b^{lm}\theta^m; & if \ 0 < m \leq l \end{cases} \tag{A6}$$

where

$$b^{lm} = \frac{(-1)^m}{2^{|m|}|m|!}\sqrt{(\frac{2l+1}{4\pi})[\frac{(l+|m|)!}{(l-|m|)!}]}. \tag{A7}$$

To be clear, θ^2 and $\theta^{|m|}$ in eq. (A6) represent power of θ. Then we also specify $\phi_s = 0$ and substitute eqs (A4), (A6) and (A7) into eqs (A1)–(A3)

$$g^{lmk1} = \sqrt{\frac{2l+1}{4\pi}} \delta_{m0} f_r \delta_{kk_s} \tag{A8}$$

$$g^{lmk2} = \frac{1}{2}\sqrt{\frac{2l+1}{4\pi}}[-f_\theta(-\delta_{m-1} + \delta_{m1}) + i f_\phi(\delta_{m-1} + \delta_{m1})]\delta_{kk_s} \tag{A9}$$

$$g^{lmk3} = \frac{1}{2}\sqrt{\frac{2l+1}{4\pi}}[i f_\theta(\delta_{m-1} + \delta_{m1}) + f_\phi(-\delta_{m-1} + \delta_{m1})]\delta_{kk_s}. \tag{A10}$$

We then substitute each one of the three independent single forces (the vertical force $f_r = 1.0$, radial force $f_\theta = 1.0$ and transpose force $f_\phi = 1.0$) into eqs (A8)–(A10) and run DSM to obtain their Green's functions.